Applied Thermal Engineering 295 (2026) 130683

Contents lists available at ScienceDirect

Applied Thermal Engineering

journal homepage: www.elsevier.com/locate/apthermeng

Research Paper

Electrochemical additive manufacturing-based cold plate with distributed inlet nozzles and outlet slots for high-power-density electronics cooling

Sangram Kumar Samal [a], Pang-Chieh Yu [a], Hsien-Chun Chang [a], Yogesh Fulpagare [b,c], Ian Winfield [d], Michael Matthews [d], Himanshu Pokharna [e], Chi-Chuan Wang [a,*]

[a] Department of Mechanical Engineering, National Yang Ming Chiao Tung University, Hsinchu, Taiwan
[b] Cooler Master Co. Ltd., Taiwan
[c] Department of Mechanical and Aerospace Engineering, The University of Texas at Arlington, TX, USA
[d] Fabric8Labs, Inc., San Diego, CA, USA
[e] Deep Materials Inc., Saratoga, CA, USA

ARTICLE INFO

Keywords:
Liquid cooling cold plate
Thermal interface material
Thermal design power
Temperature uniformity
Direct-to-chip cooling
Thermal management of data center

ABSTRACT

The rapid growth of AI, 5G, and high-performance computing has created a critical need for effective cooling of high-power-density processors, as traditional air-cooling methods struggle to dissipate heat from chips at power levels of around 1000 watts. To address this challenge, this study presents a direct-to-chip liquid cold plate with distributed inlet nozzles and outlet slots, fabricated using electrochemical additive manufacturing. The thermal performance of this cold plate is experimentally evaluated and compared with a conventional skived-fin liquid cold plate. The study focused on a single high-power chip with a 1000 W thermal load and a 30 × 30 mm^2 footprint, using a water-propylene glycol mixture as coolant, with flow rates from 0.75 to 2.5 L/min and an inlet temperature of 45 °C. Different thermal interface materials, including grease-type and soft-metal types, are examined. Results indicate that the proposed cold plate reduces thermal resistance by 8%, increases the heat transfer coefficient by 6%, reduces pressure drop by 34%, and improves temperature uniformity compared to the referenced design. Using soft metal thermal interface material further decreases thermal resistance by 11%. Overall, the cold plate requires 60% less pumping power to achieve a maximum thermal resistance of 0.032 °C/W. Beyond absolute cooling performance, the novelty of this work lies in integrating a distributed inlet–outlet design with manufacturing-ready fabrication, providing a scalable, experimentally validated platform for future high-power single-chip cooling designs. This approach emphasizes manufacturing-driven innovation, enabling flexible, high-performance cold plate designs for advanced electronic systems and data centers.

1. Introduction

Rapid growth in high-performance computing (HPC) technologies has significantly reshaped modern data centers, driven by artificial intelligence, large-scale data handling, cloud services, and the Internet of Things [1,2]. One significant consequence of technological advancement is increased heat generation from the processor [3]. For instance, recent accelerator modules such as the NVIDIA GB200 and GB300 Superchips, based on the Blackwell architecture, exhibit module-level thermal design powers (TDPs) exceeding 1 kW [4,5]. High power densities in data centers, often exceeding 30–40 kW per rack, pose challenges for traditional air-cooling systems, which struggle to maintain safe operating temperatures. While increased airflow can mitigate heat, it often increases energy consumption and reduces operational efficiency [6,7]. Direct-to-chip liquid cooling (DLC) has emerged as a viable solution, providing three to five times the heat removal efficiency of conventional air cooling by targeting the chip level [8,9]. Among DLC methods, single-phase cold plates are widely used in modern data centers, effectively managing thermal loads from GPUs and CPUs by circulating liquid coolant through microchannels or finned structures [10,11]. This approach ensures accurate thermal management, maintains consistent component temperatures, and reduces energy consumption related to cooling. Direct-to-chip cooling, particularly through liquid cold plates, is crucial for next-generation data centers that utilize ultra-high-power processors. This technology addresses thermal challenges while supporting sustainability and operational efficiency goals in the data center industry [12,13].

* Corresponding author.
E-mail address: ccwang@nycu.edu.tw (C.-C. Wang).

https://doi.org/10.1016/j.applthermaleng.2026.130683
Received 24 November 2025; Received in revised form 13 March 2026; Accepted 18 March 2026
Available online 21 March 2026
1359-4311/© 2026 Elsevier Ltd. All rights are reserved, including those for text and data mining, AI training, and similar technologies.

Nomenclature

A_{heated}	heated surface area or footprint (m^2)
C_p	specific heat (J/kg·K)
h_{app}	apparent heat transfer coefficient ($W/m^2·K$)
$MATD$	mean absolute temperature deviation (K)
Δp	pressure drop (Pa)
PP	pumping power (W)
PP^*	normalized pumping power (W/m^2)
Q	total heat input (W)
Q_{fluid}	effective heat carried out by the fluid (W)
$R_{c\text{-}in,avg}$	average case-to-inlet thermal resistance (K/W)
$R_{c\text{-}in}$	case-to-inlet thermal resistance (K/W)
$R_{c\text{-}in,max}$	maximum case-to-inlet thermal resistance (K/W)
$R^*_{c-in,avg}$	normalized average case-to-inlet thermal resistance ($K·m^2/W$)
$T_{c,avg}$	average case temperature (K)
T_{bulk}	bulk mean fluid temperature (K)
T_c	case temperature (K)
T_{in}	fluid inlet temperature (K)
T_{out}	fluid outlet temperature (K)
$T_{c,max}$	maximum case temperature (K)
$T_{c,min}$	minimum case temperature (K)
V	volumetric flow rate (L/min)

Greek symbols

ρ	density (kg/m^3)

Cold plates serve as essential heat-removal components in direct liquid cooling (DLC) systems designed for high-power electronics in data centers and typically utilize microchannel-based configurations. Since the pioneering work of Tuckerman and Pease [14], microchannel heat sinks have been widely adopted due to their high surface-area-to-volume ratio and strong convective heat transfer capability. The conventional cold plate consists of a cover plate with inlet and outlet ports for liquid coolant, along with a base plate with rectangular channels or pin-fin structures, affixed with CPUs or GPUs using a layer of thermal interface material [15–17]. Most liquid cold plates in data centers use parallel finned microchannels, commonly fabricated via CNC machining or skiving [18–20]. Experimental studies have demonstrated their effectiveness for high-power-density cooling: skived-fin cold plates can dissipate substantial heat loads while maintaining low thermal resistance [21], and optimized operational strategies can significantly improve energy efficiency in data centers [22]. These studies confirm the maturity and effectiveness of conventional microchannel cold plate cooling for data center thermal management. While parallel-skived-fin designs remain prevalent due to their reliability and established manufacturing processes, recent research focuses on enhancing thermal–hydraulic performance through structural optimization and advanced design methodologies due to the need for even higher heat flux dissipation. Modifications to microchannel geometries, including variable cross-sections, fin-pitch adjustments, and multi-layer configurations, have shown improved heat transfer efficiency, though sometimes at the cost of increased pressure drop or reduced fin effectiveness [23,24]. Furthermore, advanced manufacturing techniques, including diffusion bonding, have facilitated the development of multi-layer cold plate designs that enhance thermal performance while maintaining comparable hydraulic penalties [24]. Additionally, numerical modeling and simulation studies indicate that optimized channel layouts and flow configurations can lower cooling power requirements and improve overall system efficiency [25]. Comparative analyses highlight the need to balance thermal performance with pumping power, reinforcing the continued importance of design innovation in liquid-cooling systems [26].

Recent studies have explored geometric modifications and advanced flow-distribution strategies to address the increasing heat flux in high-power electronics, as conventional skived-fin cold plates often suffer from non-uniform temperature distribution and high pressure drops due to narrow microchannels. To address these issues, Huber and Viskanta [27] introduced an advanced cooling system that utilizes multi-nozzle jet impingement with a distributed inlet and outlet configuration. This system features adjacent inlet nozzles and exit holes for spent fluid, optimizing flow paths and reducing thermal and hydraulic boundary layers. As a result, it achieves better heat transfer efficiency, lower pumping power, reduced thermal resistance, and more uniform distribution of temperature across the heated surface. The introduction of distributed inlet nozzles and exit holes has garnered significant recognition among researchers as an advancement in liquid-cooling solutions [28–41]. Building on this concept, several studies have investigated distributed inlet-outlet jet impingement configurations to enhance thermal performance and improve temperature uniformity. Brunschwiler et al. [42] developed an innovative submerged liquid-jet-impingement cold plate featuring micron-sized nozzles and a well-distributed return manifold, achieving highly uniform cooling without the need for a base plate or thermal interface materials. Rattner [43] showed that incorporating extraction ports in jet arrays mitigates flow maldistribution and pressure losses, although the study was limited to idealized configurations. Hybrid approaches combining jets and microchannels have also been explored to balance thermal resistance and pumping power [44]. Wei et al. [45] demonstrated cost-effective polymer-based multi-jet cooling systems with competitive thermal performance, highlighting the potential of alternative materials and simplified fabrication routes. Additive manufacturing has further expanded the design space for distributed jet impingement cooling. Wei et al. [46] and Moloudi et al. [47] demonstrated that 3D-printed polymer and metal jet impingement coolers can effectively dissipate high heat loads in large-die and automotive electronics, respectively. Enhancements such as micro pin-fins on the rear side of the chip [48] and compact, lid-compatible jet manifolds with distributed inlets and outlets [49] had further improved heat transfer performance and temperature uniformity. Distributed jet impingement has also been extended to multi-chip and 2.5D high-performance computing packages, where Patel et al. [50] highlighted its effectiveness in managing high total power dissipation while maintaining acceptable pressure drops. Collectively, these studies demonstrate the strong potential of distributed inlet–outlet jet impingement for high-power cooling, while also indicating that most existing implementations focus on direct or bare-chip cooling rather than fully integrated cold plate architectures.

While conventional liquid cold plates and jet-impingement cooling modules are typically fabricated by machining, skiving, or conventional metal additive manufacturing, these approaches have limitations for producing highly detailed internal geometries with small feature sizes. Electrochemical additive manufacturing (ECAM) has recently emerged as a promising alternative for fabricating intricate cold plate structures with improved geometric resolution and surface quality [51]. Unlike laser-based or binder jet metal additive manufacturing, ECAM relies on electrodeposition, enabling finer feature control and smoother surfaces suitable for high-performance electronic cooling applications. Minimum feature sizes on the order of tens of micrometers can be achieved, making ECAM particularly attractive for optimized cold plate designs. Recent studies have demonstrated the feasibility of fabricating functional cold plate components using ECAM, highlighting its potential for direct-to-chip liquid cooling in data center environments [52,53].

A comprehensive review of existing literature indicates that

distributed inlet-outlet configurations in cold plates can significantly improve coolant distribution, reduce thermal resistance, and enhance temperature uniformity, making them particularly effective for high-power electronics cooling. However, most prior research on distributed inlet–outlet designs has focused on bare-chip cooling, often using water as the working fluid and simplified heating blocks, rather than integrating the concept into a full cold plate structure. Consequently, there is a need for manufacturable, experimentally validated cold plates that implement the distributed inlet–outlet principle. In previous studies [54,55], our research focused on the distributed inlet-outlet jet impingement cold plate (DIOJIC-CP), which underwent numerical analysis and demonstrated superior performance when compared to conventional skived-fin cold plates, particularly in terms of thermal resistance and pumping power. Motivated by these prior numerical

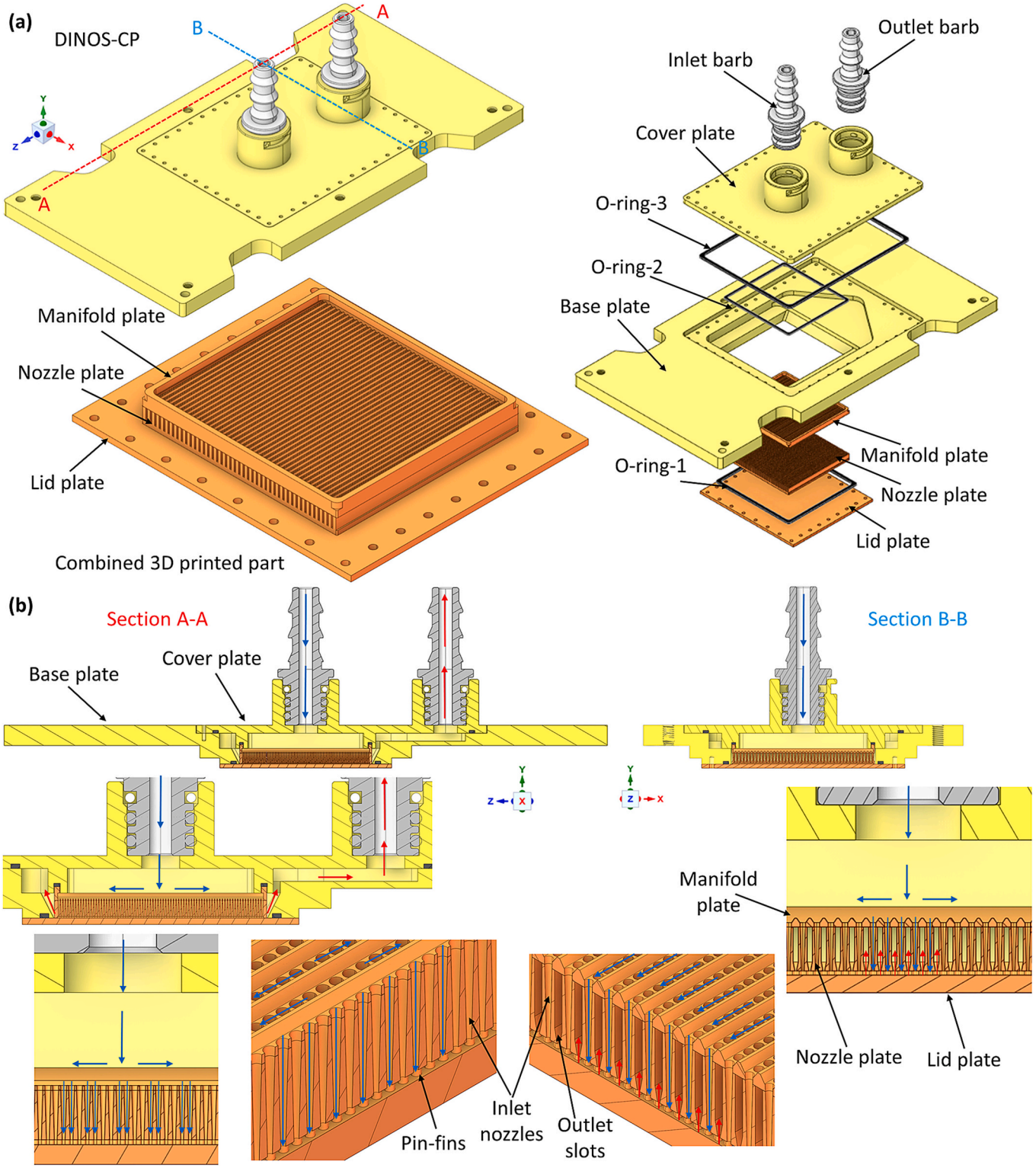


Fig. 1. Detailed schematics of the DINOS-CP, featuring isometric, sectional, and exploded views that illustrate the components of the cold plate and the fluid flow configuration.

investigations, this study presents the Distributed Inlet Nozzles and Outlet Slots Cold Plate (DINOS-CP). In contrast to our earlier work, which focused exclusively on the numerical analysis of the DIOJIC-CP with a straight inlet–outlet nozzle configuration, the current research introduces a significantly revised DINOS-CP geometry that incorporates converging inlet nozzles and diverging outlet slots. This new design has been specifically tailored for compatibility with ECAM 3D printing and has undergone experimental validation. The ECAM-compatible DINOS-CP aims to further minimize pressure drop while simultaneously enhancing thermal performance. This study addresses the limitations of prior research by integrating the distributed inlet-outlet concept with an experimentally validated, ECAM-compatible cold plate design that is ready for fabrication. This development represents a significant advancement for practical high TDP applications in electronic cooling, utilizing safe and commonly used coolants in data centers such as PG25. The overall thermo-hydraulic performance of DINOS-CP is being experimentally investigated to effectively dissipate a TDP of 1000 watts from a TTV, extending our earlier multi-heat-source numerical investigations to an experimentally validated single-heat-source configuration. By integrating design, fabrication, and experimental investigation, this research presents a comprehensive methodological framework for the cooling of high-power-density electronics. Performance is benchmarked against conventional designs and the existing literature, providing practical insights into scalable, manufacturable cold plate solutions. This approach advances the field of electronic thermal management and supports energy-efficient operation of modern high-power devices.

2. Design overview

2.1. Cold plate design

This work introduces an innovative liquid-cooling solution specifically engineered to efficiently manage the heat generated by electronic chips with a TDP of 1000 watts or greater. The cold plate, designated as the Distributed Inlet Nozzles and Outlet Slots Cold Plate (DINOS-CP), features an innovative distributed design comprising inlet nozzles and outlet slots. This new design represents a significant advancement over our prior model, the Distributed Inlet-Outlet Jet Impingement Cooling Cold Plate (DIOJIC-CP) [54], which was primarily investigated numerically. In contrast to the earlier configuration DIOJIC-CP, which used straight inlet and outlet nozzles, the present design incorporates converging inlet nozzles and diverging outlet slots. This modification improves flow distribution, enhances local convective heat transfer, and reduces pressure drop, thereby yielding superior thermo-hydrodynamic performance.

Fig. 1 illustrates the schematics of the isometric, sectional, and exploded views of the DINOS-CP. The DINOS-CP comprises five principal components: (i) nozzle plate, (ii) manifold plate, (iii) lid plate, (iv) base plate, and (v) cover plate, as detailed in Fig. 1. The illustration also provides information on the flow configurations and the arrangement of inlet nozzles and outlet slots within the cold plate. The coolant enters the cold plate through the inlet and is distributed within the manifold plate. The fluid then passes through an array of converging inlet nozzles and impinges into a cavity region located beneath the nozzle plate. Following the impact on the upper surface of the lid plate within the cavity region, the heated coolant is guided through adjacent diverging outlet slots into the outlet plenum in the base plate and subsequently exits the cold plate. This distributed design of the inlet nozzles and outlet slots significantly reduces the fluid flow length within the cavity, thereby enhancing thermal performance and minimizing pressure drop. The inclusion of micro-scale pin fins within the cavity region further augments heat transfer by increasing surface area and promoting local flow mixing.

Building on the overall flow configuration illustrated in Fig. 1, the nozzle plate serves as the primary element regulating coolant distribution and thermal performance within the cavity region. As depicted in Fig. 2, the underside of the nozzle plate features a cavity populated with an array of cylindrical micro-pin fins that extend toward the lid plate. The strategic positioning of the pin-fins on the nozzle plate ensures that a column of pin-fins is centrally positioned between a column of inlet nozzles and an outlet slot. The upper surface of the nozzle plate features straight fin channels that facilitate the systematic collection of the heated coolant after it impacts the lid plate. Along the length of each fin, several converging inlet holes are strategically distributed to deliver coolant from the manifold plate into the cavity region with controlled momentum. Additionally, the straight fins are surrounded by several diverging outlet slots that transport heated coolant from the cavity to the outlet plenum in the base plate. This comprehensive arrangement of converging inlet nozzles, pin fins, and diverging outlet slots ensures uniform flow distribution, and suppresses localized hot spots, thereby promoting enhanced heat transfer and improved temperature uniformity across the heated surface.

The manifold plate and lid plate primarily facilitate uniform coolant distribution to the inlet nozzles and serve as the interface between the cold plate and the heated surface, respectively. While these components are essential for the overall operational efficacy of the system, the specific geometrical features of these elements are secondary to the fundamental thermal mechanisms discussed herein. For clarity and conciseness, detailed geometrical dimensions and component-level specifications for the nozzle plate, manifold plate, and lid plate are provided in Section S1 of the Supplementary Information, along with a summary table of key dimensions (Table S1).

2.2. Fabrication utilizing ECAM 3D printing

The manifold plate, nozzle plate, and lid plate of the DINOS-CP are fabricated as a single unit using Electrochemical Additive Manufacturing (ECAM), a metal 3D printing method that allows high-resolution deposition of copper (99.95% purity) components with complex internal geometries [51,53]. ECAM is considered for this work because it enables the precise fabrication of intricate features such as converging inlet nozzles, diverging outlet slots, and micro pin-fins, which are challenging to produce using conventional machining or alternative additive manufacturing techniques. By utilizing a water-based copper ion feedstock and a microelectrode array printhead, ECAM achieves micron-level resolution (33 μm voxel size), high material density, and excellent surface quality (surface finish Ra below 1.3 μm), making it well-suited to realize the optimized thermo-hydraulic design of the cold plate. The ECAM-deposited copper has a thermal conductivity of 380 W/m·K and an ultimate tensile strength of 310–379 MPa. After the 3D-printed component is completed, additional machining is performed to create screw holes in the lid plate. The fully assembled DINOS-CP integrates this 3D-printed part with the base plate and cover plate, both fabricated from brass via CNC machining. O-rings and fasteners ensure a leak-proof seal at three junctions: (i) between the bottom of the base plate and the lid plate, (ii) at the manifold plate, slightly elevated above the inlet manifold chamber to facilitate a press-fit with the cover plate using an O-ring, and (iii) between the base plate and the cover plate, as illustrated in Fig. 1. The 3D-printed component is inserted into the base plate from the bottom and covered by the cover plate on top, leaving only the underside of the lid plate visible. Fig. 3 shows the integrated 3D-printed unit comprising the manifold, nozzle, and lid plates, while Fig. 4 presents the complete assembly of the DINOS cold plate. The red rectangle indicates the heated section, which will interface with the TTV heated surface using TIM. The details regarding the TTV and the test section will be elaborated upon in the subsequent section.

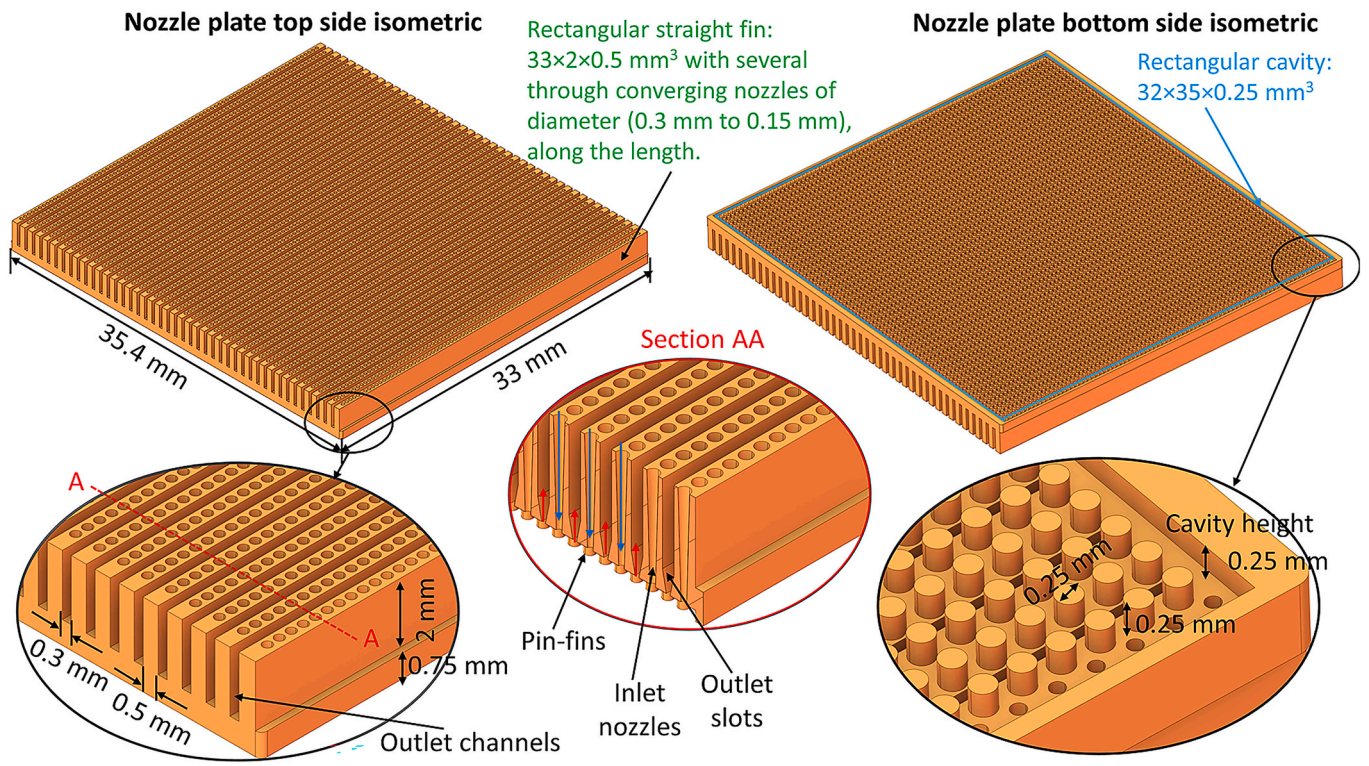


Fig. 2. Schematic representation of nozzle plate, highlighting cavity zone, pin-fins, outlet channels, and configurations of inlet converging nozzles and diverging outlet slots.

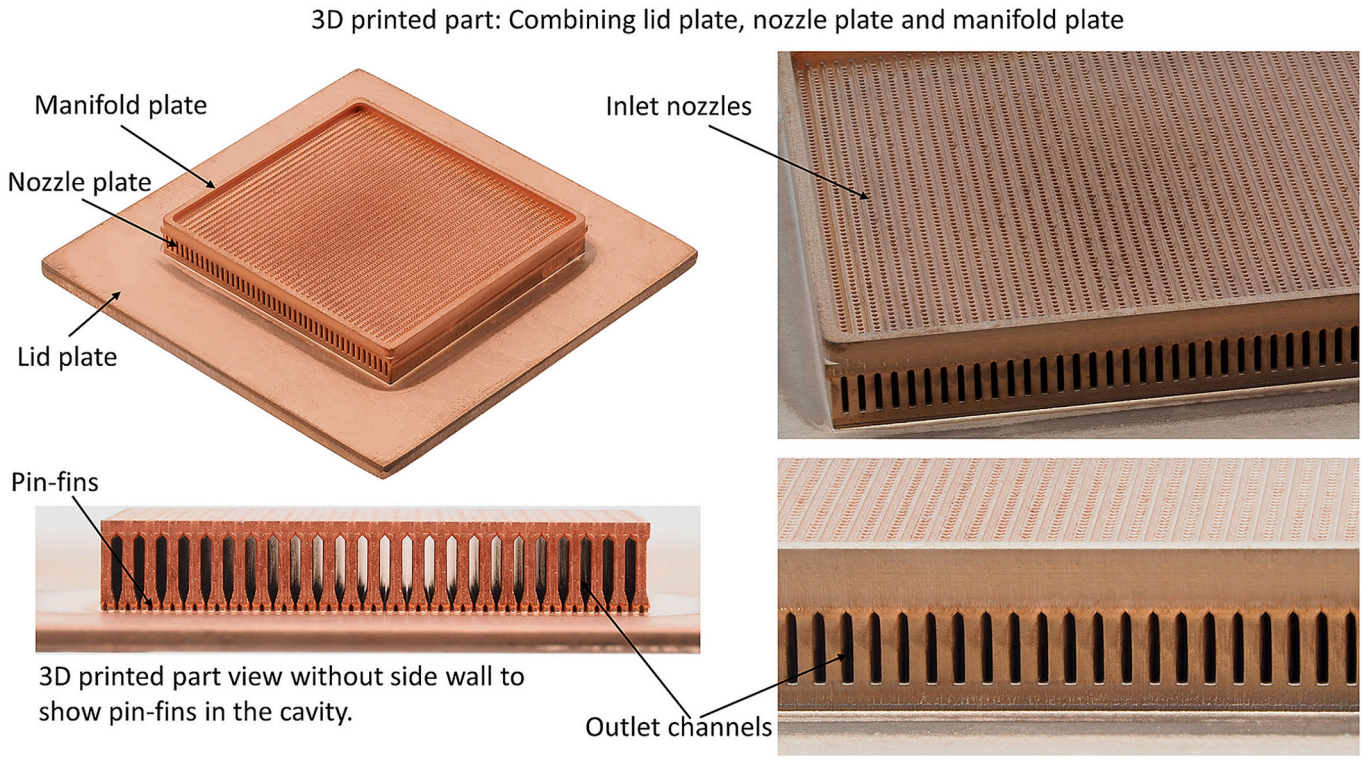


Fig. 3. 3D printed part integrating lid plate, nozzle plate, and manifold plate, fabricated using ECAM 3D printing.

3. Experimental methodology

To assess the thermo-hydraulic performance of the fabricated DINOS-CP, a comprehensive experimental investigation is conducted. Moreover, a comparative study has been conducted between the DINOS-CP and SF-CP, serving as the baseline reference. The SF-CP consists of a base plate, skived fin plate, and cover plate with inlet and outlet barbs. The skived fin plate contains multiple straight microchannels formed by

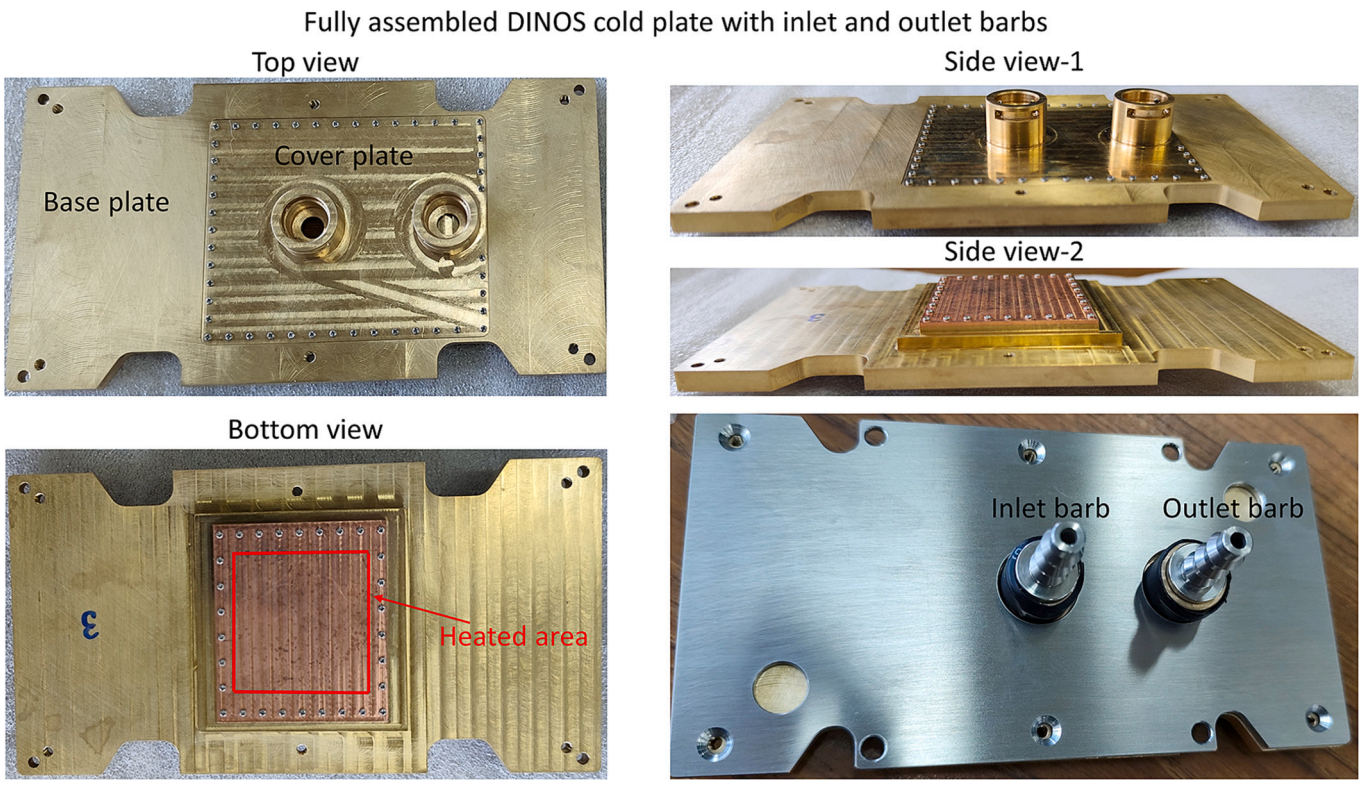


Fig. 4. Complete assembly of the DINOS cold plate, including inlet/outlet barbs.

skived fins with a thickness of 0.15 mm and a height of 2 mm, creating uniform flow passages with a width of 0.15 mm. The outer structure of the SF-CP is similar to that of the DINOS-CP, allowing a fair comparison between the innovative design and the baseline commercial product. Detailed schematics of the SF-CP are provided in the Supplementary Information (Fig. S3). The subsequent subsections provide a comprehensive overview of test section configuration, the components of the experimental loop, the instrumentation employed, as well as the methodologies utilized for data reduction and uncertainty analysis.

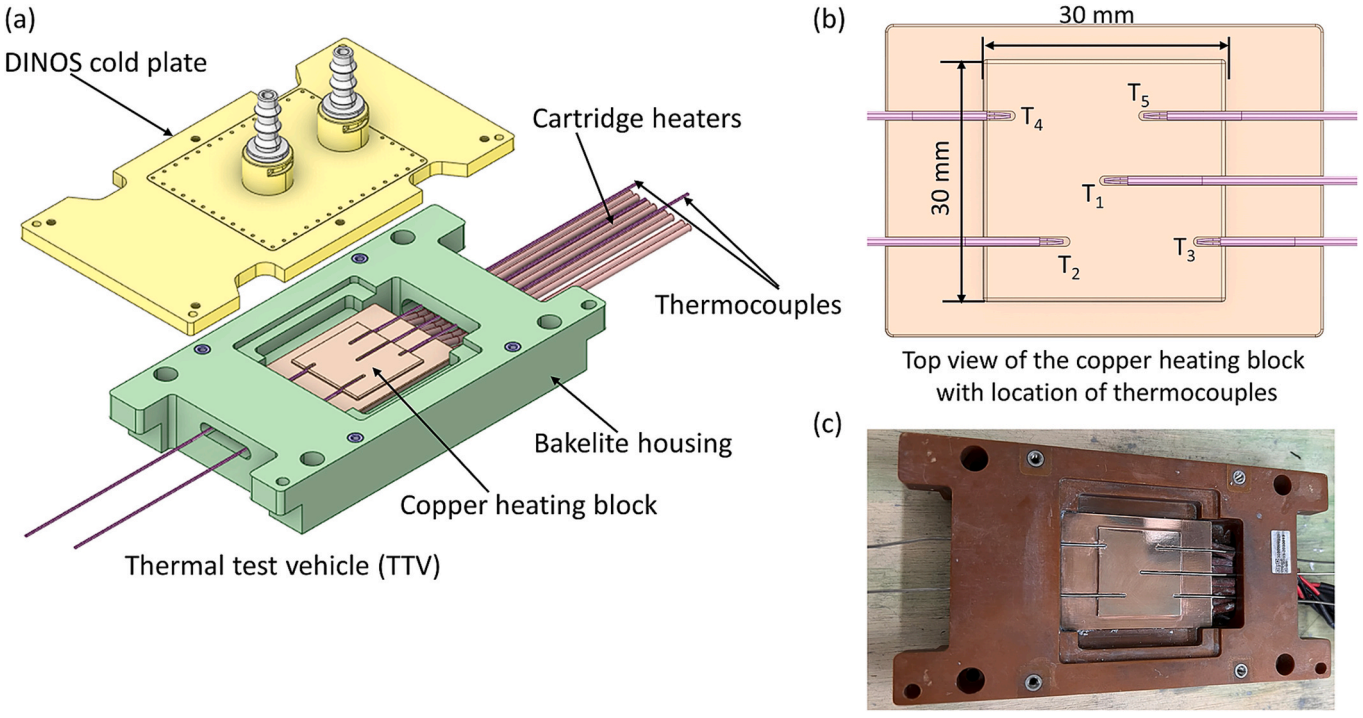


Fig. 5. Test section description: (a) schematic of the exploded views of the cold plate and TTV, (b) heater block with location of thermocouples, and (c) the thermal test vehicle (TTV).

3.1. Test section description

The test section, illustrated in Fig. 5, comprises a DINOS cold plate mounted on a TTV. This TTV is equipped with a copper heating block that incorporates four 300 W cartridge heaters. The copper block is enclosed within a Bakelite insulation housing, which serves to minimize heat losses and ensure that heat is primarily directed to the TTV heating zone. The TTV features a single heating zone measuring 30 × 30 mm^2, with the cold plate securely affixed using fasteners and a stiffener plate. The bottom side of the cold plate is meticulously positioned to match the heating zone, and a TIM is applied between the cold plate and the TTV to enhance thermal contact and mitigate interfacial thermal resistance. Two types of TIMs are utilized in separate experiments: a grease-type TIM, designated CryoFuze7 [56], claiming a thermal conductivity of 14 W/m·K, and a soft metal TIM, known as FlexiMetal [57], demonstrating a thermal conductivity of 35 W/m·K. In both cases, an initial TIM thickness of 0.2 mm is employed to ensure uniform coverage across the heated surface. This thickness is critical, as it prevents direct contact between the thermocouple tips and the cold plate base; the thermocouples are intended to measure the temperature of the heated surface rather than that of the cold plate itself. The comparison between the lower-conductivity grease TIM and the higher-conductivity soft metal TIM facilitates an evaluation of the impact of interfacial thermal resistance on the heated surface temperature and overall heat transfer performance. In accordance with the OCP guideline 2023 for the 1 kW OAM TTV design [58], a single thermocouple is positioned at the center of the heating zone earlier. However, a single sensor is insufficient for capturing the center, average, and maximum surface temperatures simultaneously. Numerical simulations of both cold plates are conducted to identify the hotspot region, revealing that it is located far from the center of the heated surface (see Fig. S5 in Section S3 of the Supplementary Information). Based on the temperature contour plots, five thermocouples are strategically placed on the heated surface to measure the center, average, and maximum surface temperatures of the TTV. They are embedded in grooves of the TTV surface and covered with a TIM layer to minimize thermal contact interference. This design ensures optimal thermal contact while accurately capturing localized surface temperatures. A direct comparison between the numerical model and experimental measurements shows good agreement in average surface temperature, confirming the model's suitability for guiding thermocouple placement (see Supplementary Information, Section S3). Ultimately, the performance of the newly designed DINOS cold plate is evaluated experimentally and subsequently compared with a reference SF-CP. This comparative analysis, in conjunction with measurements using different TIMs, highlights the effectiveness of the DINOS design in improving overall heat transfer performance compared to conventional cold plate designs.

3.2. Flow loop and instrumentation

The schematic layout of the experimental setup utilized to assess the thermo-hydraulic performance of the DINOS-CP is illustrated in Fig. 6. The test facility is constructed as a closed-loop circulation system, comprising circulating water bath, flow meter, test section, pump, data acquisition (DAQ) system, differential pressure transducer (DPT), DC power supply, and desktop computer. A comprehensive specification of all components employed in the experimental arrangement is presented

Table 1
Information regarding the equipment utilized in the experiment [54].

Equipment	Make and Model
Data acquisition system	Yokogawa, MX100
Pump	GOOD Pumps, 12 V DC 72 W, Maximum capacity 6 L/min
Differential pressure transducer	Yokogawa, EJA110A (Range: 0–98 kPa, ±0.065% of span)
Flow meter	Yokogawa, AXF005G (Range: 0.12–11.78 L/min, ±0.35%)
Circulating coolant bath	LENON Instruments, J-610 (−10 °C to 90 °C, ±0.1 °C)
DC power source	NICE-POWER, R-SPS630–232, Output: 0-60 V / 0-30 A
Thermocouples	T-type (probe), ±0.1 °C

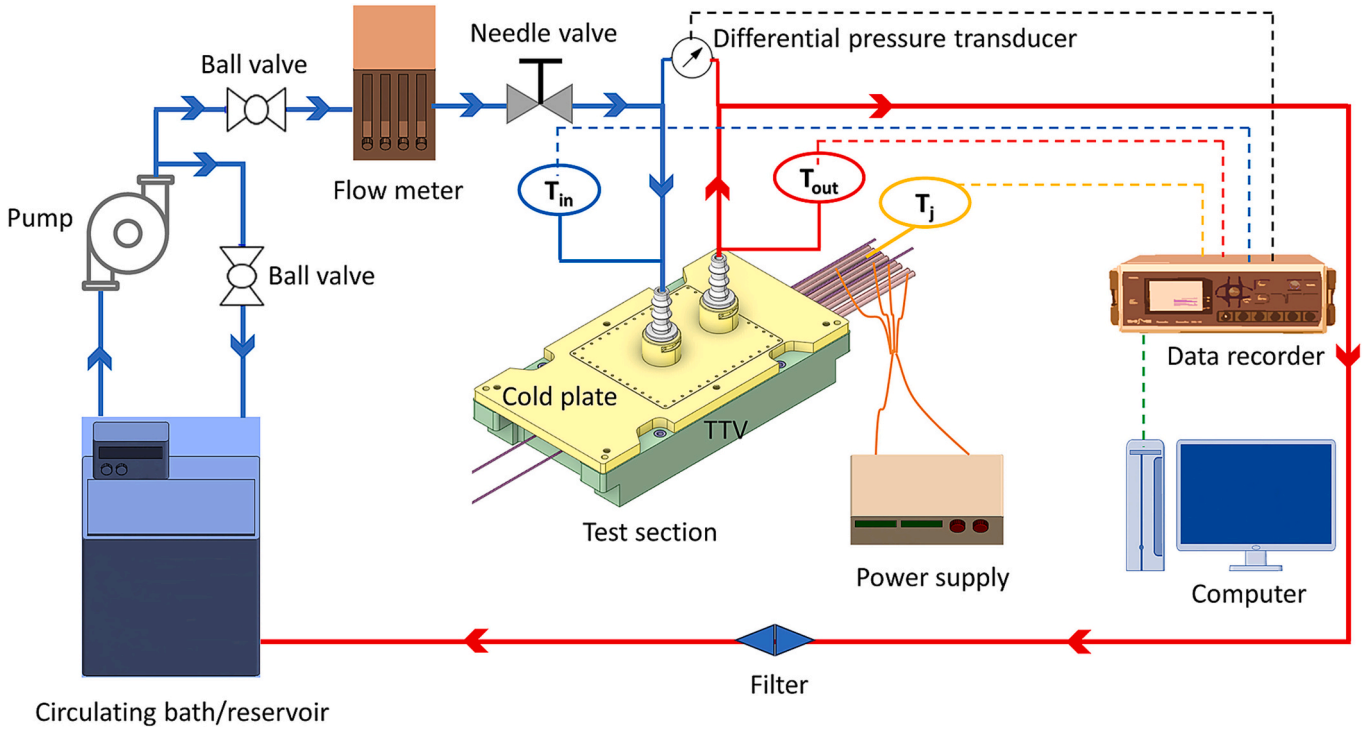


Fig. 6. Schematic diagram of the experimental configuration used to assess the thermo-hydraulic performance of DINOS-CP.

in Table 1. Information regarding the equipment utilized in the experiment. The DC power supply delivers electrical power to cartridge heaters integrated within the heating block of the TTV, facilitating the generation of a uniform and controlled heat flux. The heated copper block is encased within a Bakelite insulation housing to mitigate heat losses to the environment and ensure precise thermal measurements. The coolant used in all experiments consists of a propylene glycol–water mixture (PG25) supplied from a circulating, temperature-controlled coolant bath. The coolant is introduced into the test section at a controlled inlet temperature of 45 °C and a specified volumetric flow rate, regulated by an integrated pump. After traversing the heated surface and absorbing heat from the cold plate, the coolant returns to the water bath, where it is reconditioned to the designated temperature before being recirculated. T-type thermocouples are implemented to measure temperatures at both the inlet and outlet of the cold plate, as well as on the heated surface of the TTV. The DPT continuously records the pressure drop across the cold plate, while the flow meter quantifies the instantaneous volumetric flow rate of the coolant. All temperature, pressure, and flow data are monitored in real-time via the DAQ system, and the measurements are transferred to a desktop computer for further processing and analysis. The experiments are carried out under a constant heat load of 1000 W while systematically varying the inlet volumetric flow rate within the range of 0.75 L/min to 2.5 L/min. This range of operating conditions enables the investigation of both the thermal and hydraulic characteristics of the DINOS cold plate. To ensure repeatability, each test point is recorded after steady-state conditions are attained, as verified by temperature and pressure stabilization within ±0.2 °C and ± 1%, respectively. A photograph of the complete experimental setup is provided in Fig. S6 of the Supplementary Information.

3.3. Data reduction and uncertainty analysis

In this experimental investigation, multiple critical parameters are precisely monitored under typical atmospheric conditions within the laboratory, which is maintained at a constant room temperature of 27 °C. The parameters consisted of the temperatures at the inlet and outlet of the working fluid, the pressure difference across the cold plate, the volumetric flow rate at the inlet, and the temperatures of the surfaces being heated. Data collection is conducted utilizing a DAQ system to ensure both precision and reliability. The heat input is determined by multiplying the input voltage by the current flowing through the system, thereby providing a quantifiable amount of power supplied for the experiment. It is crucial to recognize that heat can be lost through thermal interactions with the environment surrounding the test section. Consequently, the effective heat carried by the liquid coolant (Q_{fluid}) within cold plate is expected to be lower than the total heat supplied (Q). The precise quantity of heat absorbed by the coolant can be assessed as follows:

$$Q_{fluid} = \rho \dot{V} C_p (T_{out} - T_{in}) \tag{1}$$

In this context, ρ denotes the fluid density, while T_{in} and T_{out} represent the inlet and outlet temperatures, respectively. The volumetric flow rate of the fluid at the inlet is denoted by V, and C_p represents the specific heat capacity of the fluid. Heat loss is assessed by determining the difference between the total heat supplied and the actual heat transferred by the coolant. During the course of this experiment, a maximum observed heat loss of 5% was recorded.

The case-to-inlet thermal resistance (R) is determined using three representative surface temperatures collected from five strategically positioned thermocouples: the center temperature, referred as the case temperature (T_c), the average case temperature ($T_{c,avg}$), and the maximum case temperature ($T_{c,\max}$) [59]. It is important to clarify that the term “case” pertains to the heated surface of the TTV to which the thermocouples are affixed. The T_c is frequently employed in industry and in OCP documents [58,60] as the reference “case temperature” for calculating case-to-inlet thermal resistance. The maximum temperature is of particular significance, as it denotes the threshold or maximum allowable operating temperature of the chip, which directly affects both reliability and safety considerations. The average surface temperature is the mean value derived from all five thermocouple readings, thus providing a comprehensive assessment of the thermal performance across the heated region. By assessing thermal resistance using all three temperatures, this analysis encompasses both industry-standard metrics and safety-critical benchmarks while also quantifying the average thermal performance. Utilizing these temperatures, three thermal resistances are evaluated as follows:

$$R_{c-in} = \frac{T_c - T_{in}}{Q_{fluid}} \tag{2}$$

$$R_{c-in,max} = \frac{T_{c,max} - T_{in}}{Q_{fluid}} \tag{3}$$

$$R_{c-in,avg} = \frac{T_{c,avg} - T_{in}}{Q_{fluid}} \tag{4}$$

In this context, Q_{fluid} is utilized to determine the thermal resistance, rather than relying on the total heat input, Q. This method ensures that the calculated thermal resistance accurately reflects the actual heat dissipated from the heated surface, while also accounting for any losses through insulation or to the surrounding environment.

Temperature uniformity on the heated surface of the TTV is assessed using the mean absolute temperature deviation (*MATD*) metric, which serves as a measure of the deviations in the surface temperature field from the mean value. In the current experimental setup, five thermocouples have been strategically embedded within the TTV at selected locations to capture the temperature distribution across the heated area effectively. While the precise spatial minimum temperature cannot be assured through discrete sensors, the extremes among the recorded points provide a reliable indication of temperature non-uniformity. Therefore, the *MATD* is defined as the average absolute deviation of both the maximum and minimum measured temperatures from the average surface temperature. The metric is articulated as follows:

$$MATD = \frac{\left|T_{c,max} - T_{c,avg}\right| + \left|T_{c,min} - T_{c,avg}\right|}{2} \tag{5}$$

A lower MATD value indicates improved temperature uniformity and reduced hotspot severity on the heated surface. The apparent heat transfer coefficient (h_{app}) is determined by:

$$h_{app} = \frac{Q_{fluid}}{A_{heated}\left(T_{c,avg} - T_{bulk}\right)} \tag{6}$$

In this context, A_{heated} refers to the heated area of the TTV, while T_{bulk} denotes the bulk mean temperature of the working fluid, which is determined as the average of the inlet and outlet fluid temperatures. The pumping power (PP) is derived from the measured pressure drop (Δp) across the cold plate, in conjunction with the inlet volumetric flow rate (V), as expressed in the following manner:

$$PP = \dot{V} \times \Delta p \tag{7}$$

A precise estimation of uncertainty is essential for assessing the reliability of experimental results. This study examines uncertainties in measured parameters, including temperature, volumetric flow rate, and pressure drop, by addressing both random and systematic errors. Random errors arise from environmental fluctuations and noise, which are evaluated through statistical analysis of multiple readings. The standard deviation represents the random uncertainty. Systematic errors, on the other hand, originate from instrument calibration and consistent biases, and are estimated based on manufacturer specifications and calibration certificates. The combined standard uncertainty (coverage factor = 1) is calculated by propagating both random and

systematic errors using the root-sum-square method. Furthermore, for derived parameters such as heat absorbed by the fluid (Q_{fluid}), thermal resistance (R), mean absolute temperature deviation ($MATD$), apparent heat transfer coefficient (h_{app}), and pumping power (PP), uncertainties are propagated through functional relationships. Each variable's contribution is weighted according to its sensitivity, employing standard error propagation formulas to ensure accuracy in the assessment.

$$\frac{\Delta U}{U} = \sqrt{\left[\left(\frac{\Delta u_1}{u_1}\right)^2 + \left(\frac{\Delta u_2}{u_2}\right)^2 + \ldots + \left(\frac{\Delta u_n}{u_n}\right)^2\right]} \tag{8}$$

In this context, U denotes the derived parameter, while u_1, u_2, …, u_n represent the measured parameters that influence it. The total uncertainty associated with U is indicated by ΔU, with individual uncertainties for the measured parameters labelled as Δu_1, Δu_2, …, Δu_n. This method incorporates measurement variability and systematic limitations into the final uncertainties of derived performance parameters. A summary of uncertainties for both measured and derived parameters is presented in Table 2, covering a flow rate range of 0.75 L/min to 2.5 L/min. The uncertainties reported herein are regarded as standard uncertainties. Consequently, performance enhancements are evaluated based on consistent trends across the entire operating range, rather than isolated differences at specific points.

4. Results and discussion

The current research examines the thermo-hydraulic performance of the newly developed DINOS cold plate and conducts a comparative analysis with a conventional SF-CP, which serves as a baseline reference for performance evaluation. Experiments are performed utilizing two distinct TIMs: a grease-type TIM and a soft metal TIM. This assessment aims to evaluate their impact on surface temperature distribution, thermal resistances, and heat transfer characteristics. The coolant utilized in all experiments is PG25, supplied at an inlet temperature of 45 °C, with the TDP of test section consistently maintained at 1000 W. The initial discussion focuses on the behaviors of heated surface temperatures, including center, average, and maximum temperatures for both cold plates and thermal interface materials across a range of inlet volumetric flow rates. Subsequently, thermal performance is assessed in terms of the temperature uniformity, thermal resistances, and average heat transfer coefficient. The hydraulic performance is also analyzed, encompassing pressure drop and pumping power. Ultimately, the overall cooling performance of the DINOS cold plate is benchmarked against existing literature to underscore its relative advantages in enhancing thermo-hydraulic performance. Tests are conducted for volumetric flow rates between 0.75 and 2.5 L/min, in increments of 0.25 L/min, to capture trends in both thermal and hydraulic behaviors.

4.1. Thermal performance

This section provides a comparative assessment of the thermal performance between DINOS-CP and SF-CP. This comparison is illustrated by plotting the variations in measured surface temperatures, thermal resistances, mean absolute temperature deviations, and average heat transfer coefficients as functions of inlet volume flow rate. Additionally, this section examines the effect of different TIMs on the thermal performance of both cold plates.

Table 2
Values of uncertainty associated with different measured and calculated parameters.

Parameters	Uncertainty
Temperature	±0.3 °C
Volume flow rate	±1 mL/min to ±5 mL/min
Pressure drop	±0.04 kPa
Heat absorbed by fluid (W)	±2% to ±7%
Thermal resistance (°C/W)	±2.2% to ±7.3%
Mean absolute temperature deviation (°C)	±2% to ±3.5%
Apparent heat transfer coefficient (W/m^2 .°C)	±2.3% to ±7.1%
Pumping power (W)	±0.2% to ±0.7%

In the design of a liquid cold plate, the primary goal is to lower the chip's temperature below its maximum operational threshold. In this study, the TTV is utilized to simulate a logic chip, and the temperatures of the heated surface of the TTV are measured at various flow rates for a TDP of 1000 W. Fig. 7 illustrates the variation in case/center temperature (T_c), the maximum case temperature ($T_{c,max}$), and the average case temperature ($T_{c,avg}$) with the inlet volume flow rate (V) for both the DINOS-CP and SF-CP configurations, taking into account both grease TIM and soft metal TIM.

As depicted in Fig. 7, an increase in flow rate correlates with a decrease in surface temperatures across the four scenarios examined. This phenomenon is ascribed to the improvement of convective heat transfer. As a result, a notable decrease in the surface temperature of the heater has been observed. Specifically, when the flow rate is increased from 0.75 L/min to 2.5 L/min, the DINOS-CP utilizing a soft metal TIM achieves reductions of 17.5%, 15.9%, and 15.4% for T_c, $T_{c,\max}$, and $T_{c,avg}$, respectively. Conversely, the SF-CP employing soft metal TIM demonstrates reductions of 13.8%, 14.3%, and 14.7% for the same parameters. Note that the nominal thermal conductivity of soft metal is near 35 W/m·K, which is about 2 to 3 times higher than that of thermal grease. Hence, the TIM thermal resistance is appreciably reduced by imposing soft metal. The results indicate that the thermal resistance of TIM for liquid cooling cannot be overlooked. The data illustrated in Fig. 7 indicates that the SF-CP exhibits a lower T_c, while the DINOS-CP achieves a lower $T_{c,\max}$. Additionally, the DINOS-CP exhibits a lower $T_{c,avg}$ at flow rates exceeding 1 L/min. Overall, it can be concluded that the DINOS-CP design presents reduced heater temperatures when compared to the SF-CP. The temperature variation can primarily be attributed to the internal flow configuration present in both cold plates, which will be elaborated upon later in this section.

As presented in Fig. 7(a), the difference in T_c between the cold plates diminishes as the flow rate increases. At a flow rate of 0.75 L/min, the SF-CP with grease TIM demonstrates an 8% lower T_c compared to the DINOS-CP, whereas at 2.5 L/min, the T_c in the SF-CP decreases by 3.6% compared to the DINOS-CP. Similarly, for the case of soft metal TIM, at 0.75 L/min, the SF-CP shows a 4% reduction in T_c compared to the DINOS-CP, whereas at 2.5 L/min, the DINOS-CP slightly reduces T_c by 0.5% compared to the SF-CP. This indicates that at higher flow rates, the T_c within the DINOS-CP may be lower than that of the SF-CP. This observation holds true for the soft metal TIM case, as the DINOS-CP exhibits marginally lower T_c at flow rates exceeding 2 L/min. However, regarding the maximum case temperature, the DINOS-CP consistently displays a lower $T_{c,max}$ compared to the SF-CP, with the difference in $T_{c,max}$ between the two cold plates increasing with volume flow rate. At V = 0.75 L/min, the DINOS-CP with grease TIM achieves a $T_{c,max}$ reduction of 1.1% compared to the SF-CP. At $V = 2.5$ L/min, the $T_{c,max}$ is 3.6% lower in the DINOS-CP compared to the SF-CP. In a similar manner, for the soft metal TIM, at 0.75 L/min, the DINOS-CP achieves a $T_{c,max}$ reduction of 1.3% compared to the SF-CP, while at 2.5 L/min, it lowers $T_{c,max}$ by 2.1% in comparison to the SF-CP. The trend observed for the average case temperature varies from the patterns seen in the other two temperatures. For grease TIM, the SF-CP reveals a lower $T_{c,avg}$ (with a maximum reduction of 2%) within the volume flow rate range of 0.75–1.5 L/min, whereas beyond 1.5 L/min, the DINOS-CP exhibits a lower $T_{c,avg}$ (with a maximum reduction of 0.9%) compared to the SF-CP. Similarly, in the case of soft metal TIM, the DINOS-CP demonstrates a lower $T_{c,avg}$ beyond 1 L/min with a maximum reduction of 1.4%.

In the SF-CP design, the fluid enters via the main inlet, positioned above the central section of the skived fin plate, and impacts the skived fins before dividing into two streams that flow in opposite directions through the channels (as shown in Fig. S3 of Supplementary Information). The initial impact of the fluid on the central zone promotes

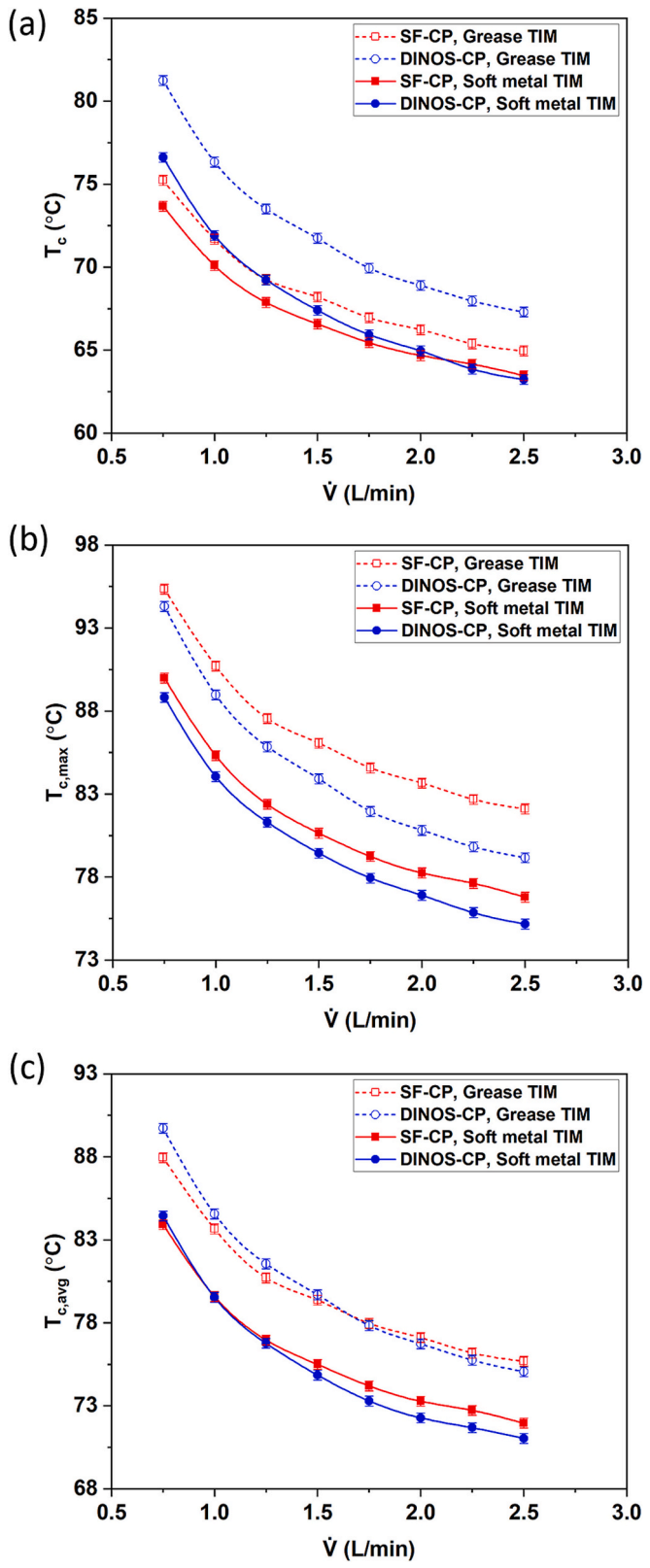


Fig. 7. Variation of the heated surface temperatures: (a) center/case temperature (T_c), (b) maximum case temperature ($T_{c,max}$), and (c) average case temperature ($T_{c,avg}$) with volumetric flow rate (V) for DINOS and SF cold plates using two different TIMs.

enhanced heat transfer due to a lower temperature gradient at that location, resulting in a reduced temperature there compared to other locations. In contrast, within the DINOS-CP, the fluid strikes the inlet chamber of manifold plate after entering through the main inlet, where it is distributed almost uniformly to all the inlet converging nozzles before entering the cavity zone and impacting the upper side of the lid plate, thereby facilitating heat removal by the fluid (see Fig. 1). Due to the uniform distribution of fluid across all inlet nozzles, the central zone on the lid plate receives a smaller fluid volume than that of the SF-CP, resulting in a higher center temperature compared to the SF-CP. This temperature observation is further supported by the temperature contours obtained from numerical simulations, as illustrated in Fig. S5 of Supplementary Information. The results indicate that the uniform flow distribution through the nozzles in the DINOS-CP correlates with a more even temperature distribution on the heated surface. However, in the SF-CP, initial fluid impact at the central zone leads to increased heat transfer in that area. As the fluid progresses downstream in the channel, the temperature gradient decreases, resulting in a reduction in the fluid's heat-carrying capacity. Thus, a hotspot region is observed near the downstream sections of the SF-CP, resulting in higher maximum temperatures in the SF-CP compared to the DINOS-CP.

The data presented in this figure indicate that the application of soft metal TIM results in significant reductions in temperature across both cold plates when compared to grease-type TIM. Specifically, the soft metal TIM achieves reductions in the critical temperatures, including T_c, $T_{c,max}$, and $T_{c,avg}$ up to 6%, 6.5%, and 6.1%, respectively. This decrease in surface temperatures can be attributed to the higher thermal conductivity of the soft metal TIM, which effectively lowers the thermal resistance of the TIM layer situated between the heater surface and the bottom surface of the cold plate. Consequently, the use of TIM with enhanced thermal conductivity proves beneficial in reducing chip temperatures.

The numerically simulated temperature contours indicate that the uniformity of temperature on the heated surface is superior in the case of the DINOS-CP compared to the SF-CP (as shown in Fig. S5 of Supplementary Information). To validate this uniformity experimentally, the mean absolute temperature deviation (*MATD*) is assessed, considering all measured temperature values. A lower *MATD* value signifies improved uniformity in temperature distribution across the heater surface. Fig. 8 presents the variation of *MATD* with the volume flow rate for DINOS-CP and SF-CP, utilizing soft metal TIM and grease TIM. The figure demonstrates that the *MATD* decreases for both types of cold plates as the volume flow rate rises. This finding indicates that the

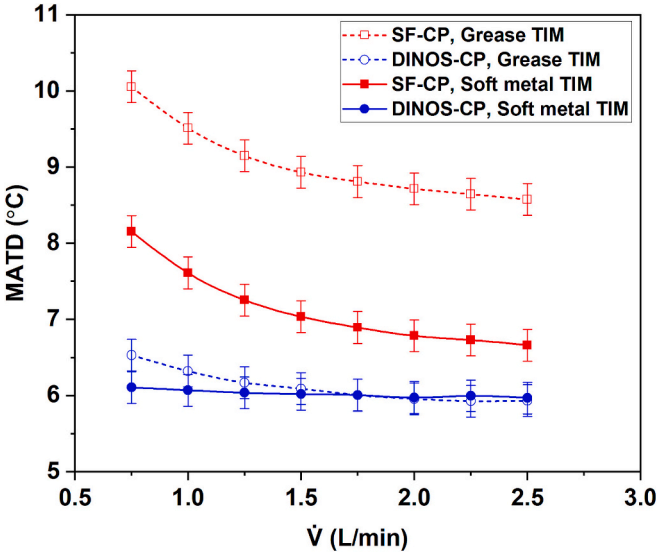


Fig. 8. Variation of the mean absolute temperature deviation (*MATD*) with volumetric flow rate (V) for DINOS and SF cold plates using two different TIMs.

uniformity of temperature distribution improves with higher flow rates. Additionally, it is observed that the DINOS-CP exhibits a notable reduction in *MATD* values compared to the SF-CP. Specifically, DINOS-CP utilizing grease TIM achieves a maximum *MATD* reduction of 35% relative to SF-CP, while it reduces *MATD* by a maximum of 25% when using soft metal TIM compared to SF-CP. This notable decrease in MATD indicates that the temperature spread across the heated surface of the DINOS-CP is more uniform compared to that of the SF-CP. This improved uniformity can be attributed to the presence of distributed inlet nozzles and outlet slots in the DINOS-CP design. The fluid distribution through each nozzle is nearly uniform, resulting in uniform distribution of fluid striking the top surface of the lid plate in the cavity region and transporting a consistent heat removal via locally effective convective heat transfer. As a result, the temperature across the heated surface becomes more consistent.

The selection of TIM significantly influences temperature uniformity, which corresponds with the thermal characteristics of the two cold-plate architectures examined. While the soft-metal TIM demonstrates considerably higher thermal conductivity compared to the grease TIM, its relative enhancement in *MATD* is notably more significant for the SF-CP, reaching up to 22%, than for the DINOS-CP, which achieves an improvement of only 6.5%. This phenomenon can be attributed to the inherent non-uniform coolant flow distribution within the SF-CP, where downstream regions experience diminished coolant momentum, resulting in the formation of localized hot spots, as supported by temperature contour analyses derived from numerical simulations. The application of soft-metal TIM effectively alleviates these localized thermal gradients by minimizing interfacial thermal resistance, thereby substantially enhancing temperature uniformity within the SF-CP. Conversely, the DINOS-CP inherently delivers a highly uniform coolant distribution due to its optimized distributed inlet nozzles and outlet slot configuration; hence, the additional advantages of utilizing a higher-conductivity TIM are comparatively less significant. These findings underscore the dominant role that cold-plate geometry plays in determining temperature uniformity, while the choice of TIM serves a secondary yet complementary function.

The relationship between case-to-inlet thermal resistance and inlet volumetric flow rate for both cold plate configurations utilizing different TIMs is presented in Fig. 9. This study evaluates case-to-inlet thermal resistance, considering three critical surface temperatures: case/center temperature (T_c), maximum case temperature ($T_{c,max}$), and average case temperature ($T_{c,avg}$). Consequently, the case-to-inlet thermal resistance ($R_{c\text{-}in}$), maximum case-to-inlet thermal resistance ($R_{c\text{-}in,max}$), and average case-to-inlet thermal resistance ($R_{c\text{-}in,avg}$) are defined according to Eqs. (2–4). These equations demonstrate that each thermal resistance is directly proportional to the corresponding temperature. It is clear that the trend in thermal resistance subject to the influence of volume flow rate mirrors the variation trends of the surface temperatures.

As illustrated in Fig. 9, an increase in volumetric flow rate results in a decrease in all thermal resistances, correlating with an enhancement in the rate of heat transfer by the fluid. The data indicate that the SF-CP configuration exhibits a lower $R_{c\text{-}in}$, whereas the DINOS-CP configuration reflects a lower $R_{c\text{-}in,\max}$. Furthermore, the DINOS-CP demonstrates a reduced $R_{c\text{-}in,avg}$ for flow rates beyond 1 L/min, suggesting its effectiveness in minimizing both maximum and average case-to-inlet thermal resistance, which are critical factors in the context of industrial cold plates. Fig. 9(a) reveals that the disparity in $R_{c\text{-}in}$ between the SF-CP and DINOS-CP diminishes as the flow rate increases. At a flow rate of 0.75 L/min, the SF-CP with grease TIM achieves a 20.8% reduction in $R_{c\text{-}in}$ compared to DINOS-CP, while at 2.5 L/min, the SF-CP still maintains a 12% advantage. Conversely, with the soft metal TIM, the SF-CP lowers $R_{c\text{-}in}$ by 10.5% at 0.75 L/min, whereas the DINOS-CP reduces $R_{c\text{-}in}$ by 2.3% at 2.5 L/min. A similar trend is also observed in the variation of T_c, as depicted in Fig. 7. The uniform flow distribution within the cold plate, along with uniform temperature distribution across heated surface, enables DINOS-CP to effectively lower the maximum heater surface

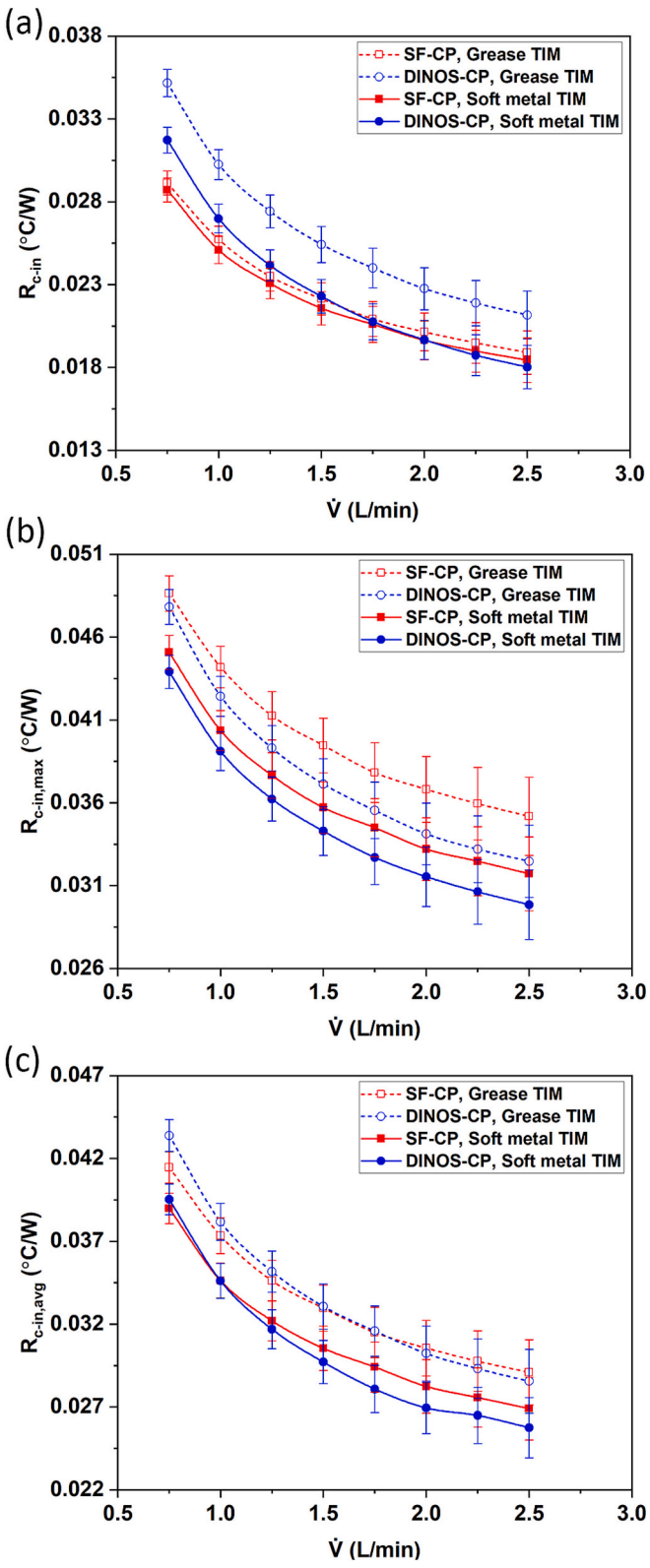


Fig. 9. Variation of case-to-inlet thermal resistances: (a) thermal resistance ($R_{c\text{-}in}$), (b) maximum thermal resistance ($R_{c\text{-}in,max}$), and (c) average thermal resistance ($R_{c\text{-}in,avg}$) with volumetric flow rate (V) for DINOS and SF cold plates using two different TIMs.

temperature, thereby achieving a reduction in $R_{c\text{-}in,max}$ of up to 8% and 6% relative to the SF-CP utilizing grease TIM and soft metal TIM, respectively. However, it is noteworthy that the trend for $R_{c\text{-}in,avg}$ differs from that of $R_{c\text{-}in}$ and $R_{c\text{-}in,\max}$. With the grease TIM, the SF-CP exhibits a lower $R_{c\text{-}in,avg}$ up to a flow rate of 1.75 L/min (with a maximum reduction of 4.6%), whereas the DINOS-CP reduces $R_{c\text{-}in,avg}$ beyond this point (with a maximum reduction of 2%). Similarly, for cases involving the soft metal TIM, the DINOS-CP achieves a reduction in $R_{c\text{-}in,avg}$ beyond 1 L/min, with a maximum reduction of 4.3%. The superior thermal conductivity of the soft metal TIM results in a lower interfacial thermal resistance, which enhances overall heat transfer and contributes to a reduction in total case-to-ambient thermal resistance. When compared to the grease TIM, the soft metal TIM can reduce $R_{c\text{-}in}$, $R_{c\text{-}in,max}$, and $R_{c\text{-}in,avg}$ by up to 15%, 10%, and 11%, respectively. In summary, the DINOS-CP combined with soft metal TIM exhibits enhanced thermal performance.

To evaluate the thermal performance of the cold plate, the apparent heat transfer coefficient (h_{app}) is assessed for both cold plate designs, with its variation concerning the flow rate depicted in Fig. 10 for two TIMs. As previously discussed, the presence of multiple distributed inlet nozzles and outlet slots in the DINOS-CP design facilitates the passage of fluid into the cavity region. This fluid effectively transports heat from the heated surface of the lid plate and exits through the adjacent slots. This flow configuration offers direct impingement with a thinner thermal boundary layer and a shorter flow length, which collectively enhance convective heat transfer within the DINOS-CP. Additionally, the incorporation of multiple cylindrical pin-fins within the cavity promotes improved flow circulation and conduction heat transfer, as these fins maintain direct contact with the lid plate. The synergistic effect of enhanced convective heat transport by the fluid and improved solid conduction heat transfer leads to an overall enhancement in the heat transfer performance of the DINOS-CP. This improvement is evident in the plot of the average heat transfer coefficient. Specifically, compared to the SF-CP, the DINOS-CP utilizing a soft-metal TIM achieves a maximum increase of 6% in h_{app}. Furthermore, the figure reveals that the implementation of the soft metal TIM results in a maximum improvement of 15% in h_{app} when compared to the grease TIM.

The evaluation of thermal performance indicates that the current DINOS-CP design demonstrates reduced heated surface temperatures, decreased thermal resistance, enhanced uniformity in temperature distribution, and improved heat transfer coefficients in comparison to the SF-CP. Moreover, the use of the soft metal TIM significantly enhances thermal performance.

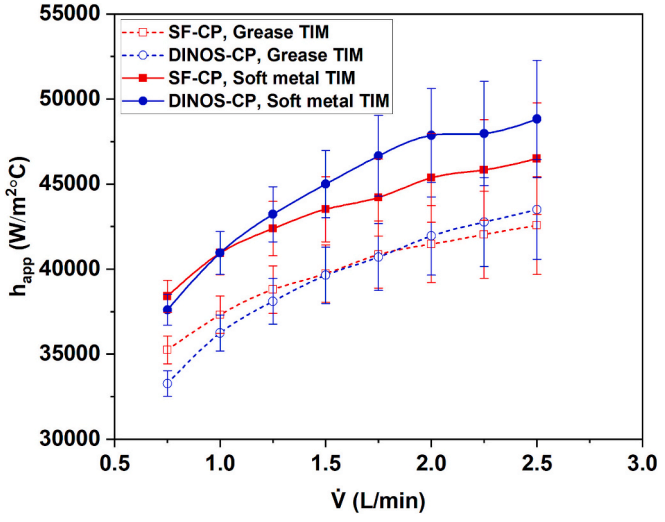


Fig. 10. Variation of the apparent heat transfer coefficient (h_{app}) with volumetric flow rate (V) for DINOS and SF cold plates using two different TIMs.

4.2. Hydraulic performance

The hydraulic performance of the cold plates is assessed by analyzing the variation in pressure drop (Δp) and pumping power (PP) across the evaluated flow rate range, as depicted in Fig. 11. This section presents a comparative examination of the pressure drop characteristics of the DINOS-CP and SF-CP for both TIMs, followed by an analysis of the corresponding pumping power requirements. This analysis aims to explain the relative hydraulic advantages of each cold plate design. The illustration clearly shows that the pressure drop in DINOS-CP and SF-CP increases with an increase in volume flow rate. This phenomenon occurs because a higher flow rate leads to greater frictional losses within the flow passages of the cold plate. As the coolant velocity increases, shear stress at the walls escalates, thereby resulting in a significant overall pressure loss across the cold plate. The figure further indicates that the current DINOS-CP design significantly reduces the pressure drop compared to the SF-CP, achieving a maximum reduction of approximately 34%. This enhancement can be primarily attributed to the flow-distribution architecture of the DINOS-CP, which utilizes multiple distributed inlet nozzles and wider outlet slots to facilitate a more uniform flow distribution and mitigate localized flow acceleration. Consequently, this design results in minimized frictional losses and avoids the high-velocity regions typically associated with the densely packed, narrow microchannels of the SF-CP. In contrast, the skived fin structure in the SF-CP results in tighter flow passages and increased shear stress along the fin surfaces, leading to a substantially greater pressure drop. A similar trend is observed in the variation of pumping power. According to Eq. (7), the pumping power is directly proportional to the pressure drop at a given flow rate; therefore, it exhibits a similar variation trend to that of the pressure drop. Due to the DINOS-CP's capacity to significantly reduce pressure drop, it concurrently necessitates reduced pumping power compared to the SF-CP, with a maximum reduction of approximately 34%. From this hydraulic performance assessment, it can be concluded that the DINOS-CP achieves the requisite cooling performance while imposing considerably lower flow impedance. However, the impact of the TIM type on hydraulic resistance is minimal. Given that the flow path and hydraulic behavior are predominantly dictated by the internal geometry of the cold plate, the choice of TIM at the solid–solid interface exerts a negligible influence on the coolant flow characteristics. Consequently, both the pressure drop and pumping power remain largely unaffected by the selection of TIM.

4.3. Overall cooling performance and benchmarking

To comprehensively assess the effectiveness or advantages of the proposed cooling solution, the overall cooling performance of DINOS-CP is compared with that of the reference SF-CP and benchmarked against relevant findings in the existing literature. This section integrates thermal and hydraulic performance analyses to present a comprehensive view of the trade-off between heat removal capability and flow resistance. To explain this trade-off, Fig. 12 illustrates the relationship between $R_{c\text{-}in,\max}$ and $R_{c\text{-}in,avg}$ with respect to pumping power for both cold plates. The data clearly indicate that the DINOS-CP exhibits lower thermal resistance and requires less pumping power compared to the SF-CP. To achieve a specific $R_{c\text{-}in,max}$ of 0.032 °C/W, the DINOS-CP requires 60% less pumping power than the SF-CP. Likewise, to attain an $R_{c\text{-}in,avg}$ of 0.027 °C/W, DINOS-CP needs only 57% less pumping power than its counterpart. These findings distinctly highlight the superior cooling efficiency of the DINOS-CP, which provides comparable thermal performance while significantly reducing hydraulic energy costs.

To thoroughly assess the efficacy of the DINOS-CP, its overall thermo-hydraulic performance is benchmarked against existing cold plates documented in the literature. The comparison involves four recent studies [46,47,49,50] that examine liquid cooling modules based on the concept of distributed inlet and outlet nozzles.

The specifications of the cold plates considered from these studies

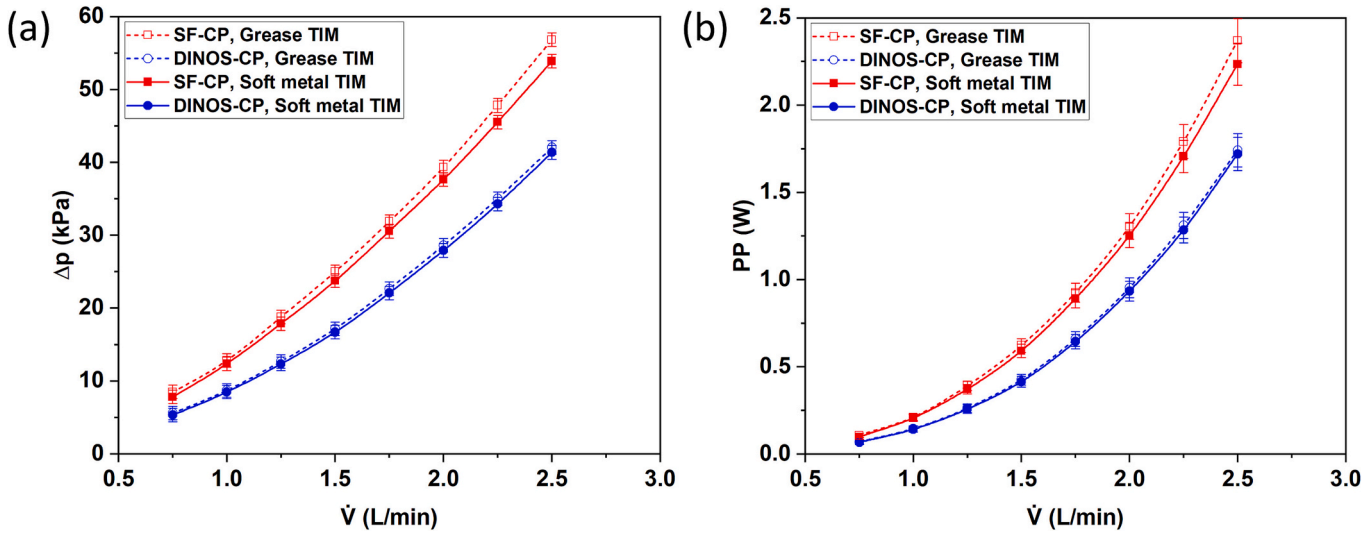


Fig. 11. Variation of (a) pressure drop (Δp), and (b) pumping power (PP) with volumetric flow rate (V) for DINOS and SF cold plates using two different TIMs. Error bars are magnified by a factor of 25 to enhance visibility.

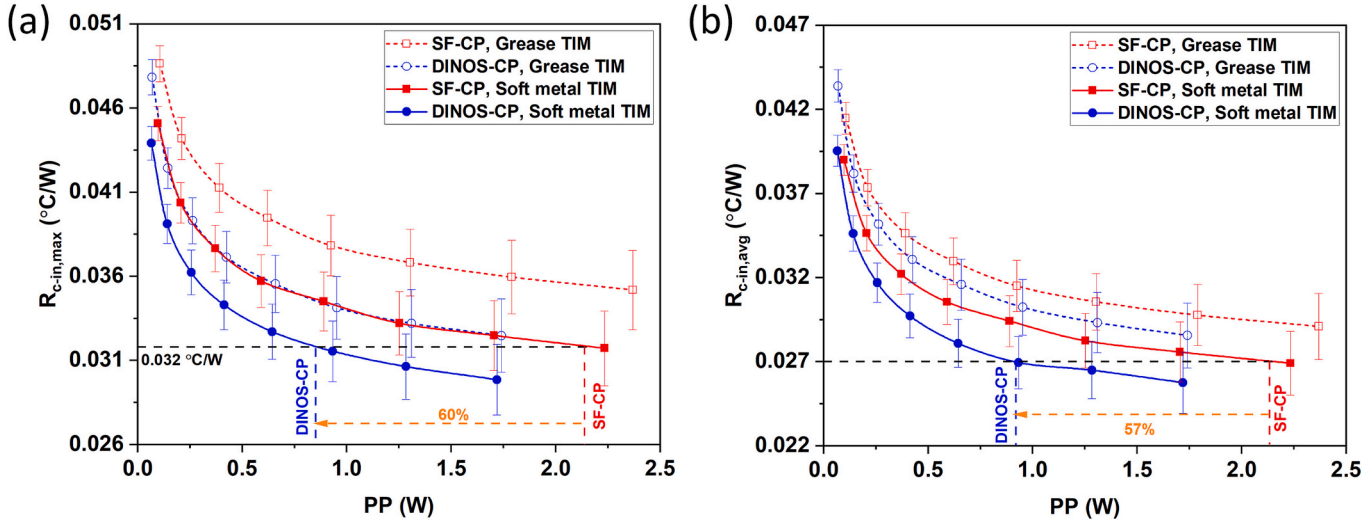


Fig. 12. Variation of (a) maximum thermal resistance ($R_{c\text{-}in,max}$), and (b) average thermal resistance ($R_{c\text{-}in,avg}$) with pumping power (PP) for DINOS and SF cold plates using two different TIMs.

Table 3
Overview of the input specifications for cold plates based on literature that are utilized for benchmarking purposes.

References	Input Parameters
Wei et al. [46]	footprint: 23 × 23 mm^2, TDP: 529 W, coolant: water, inlet temperature: 10 °C, flow rate range: 1.12 to 4.46 L/min, cooling module material: polymer
Moloudi et al. [47]	footprint: 20 × 20 mm^2, TDP: 300 W, coolant: water, inlet temperature: 20 °C, flow rate range: 0.5 to 6 L/min, cooling module material: aluminum
Sahu et al. [49]	footprint: 10 × 10 mm^2, TDP: 420 W, coolant: water, inlet temperature: not mentioned, flow rate range: 0.5 to 2.5 L/min, cooling module material: ABS-like translucent clear resin
Patel et al. [50]	footprint: 26 × 26 mm^2, TDP: 1000 W, coolant: water, inlet temperature: 20 °C, flow rate range: 1.5 to 4 L/min, cooling module material: ceramic-like high temperature resin
Present work DINOS-CP	footprint: 30 × 30 mm^2, TDP: 1000 W, coolant: PG25, inlet temperature: 45 °C, flow rate range: 0.75 to 2.5 L/min, cooling module material: copper

are presented in Table 3. It should be noted that the selected cold plates differ in footprint or heated surface area. Consequently, the comparison is conducted using normalized metrics to enable fair benchmarking. The normalized average case-to-inlet thermal resistance ($R^*_{c-in,avg}$) is calculated as $R^*_{c-in,avg} = R_{c-in,avg} \times A_{heated}$, where A_{heated} is the heated surface area. Similarly, the normalized pumping power (PP^*) is determined $PP^* = PP \,/\, A_{heated}$ for all examined cold plates [45]. These normalized quantities enable direct comparison of intrinsic cooling and hydraulic performance across cold plates of different sizes. The comparative analysis of normalized thermal resistance and normalized pumping power is presented in Fig. 13 for all the considered cold plates. This figure illustrates that the DINOS-CP outperforms the designs presented by Wei et al. [46], Moloudi et al. [47], and Patel et al. [50] by reducing thermal resistance at a lower pumping power. However, the cold plate of Sahu et al. [49] shows reduced thermal resistance compared to the DINOS-CP, but it requires more pumping power. It is noteworthy that PG25 serves as the coolant in the DINOS cold plate, while water is

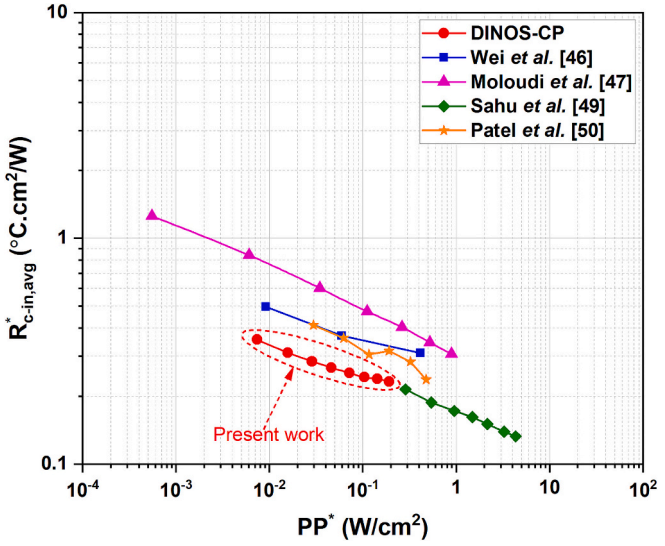


Fig. 13. Benchmarking of overall thermo-hydraulic performance of the DINOS-CP against reference cold plates from literature [46,47,49,50] using normalized thermal resistance ($R^*_{c-in,avg}$) and normalized pumping power (PP^*).

utilized as the coolant in the other examined cold plates from the literature. These benchmarking results distinctly demonstrate the significant potential of the DINOS cold plate for high-power-density electronic chip cooling applications.

From a material reliability standpoint, the copper fabricated by ECAM utilized in this study exhibits a purity level exceeding 99.95%, which is comparable to oxygen-free copper grades, such as C10200, that are conventionally employed in skived-fin cold plates. Consequently, the anticipated long-term behavior of this material is expected to align closely with that of traditional copper cold plate components utilized in data center cooling systems. During the assembly of cold plates, brazing cycles that typically exceed 800 °C may lead to the development of coarse-grained microstructures in the copper, a phenomenon also noted in the production of conventionally manufactured cold plates. In operational environments, potential long-term degradation mechanisms may encompass corrosion or erosion resulting from continuous coolant flow; however, it is important to note that data center cooling loops generally include corrosion inhibitors to alleviate such risks. Further research under conditions that accurately represent flow rates and temperatures will be essential to comprehensively assess the long-term reliability of the material.

5. Conclusions

This work presents an experimental investigation of the thermo-hydraulic performance of the distributed inlet nozzles and outlet slots cold plate (DINOS-CP), which is fabricated using ECAM-based 3D printing. Test results for DINOS-CP are compared with those of a traditional skived-fin cold plate (SF-CP), and two types of TIMs (grease and soft metal) are used for further comparison. The experiments are conducted at a heat input of 1000 W using PG25 coolant with an inlet temperature of 45 °C, across flow rates of 0.75–2.5 L/min. The results of this research reveal numerous notable advantages of DINOS-CP over the SF-CP. The key findings of this study are as follows:

- DINOS-CP demonstrated improved thermal performance, with maximum and average thermal resistances reduced by 8% and 4.3%, respectively, and temperature uniformity improved by 35% compared to the SF-CP. The apparent heat transfer coefficient increased by 6%. The enhanced thermal performance is due to distributed inlet nozzles and outlet slots, which promote uniform coolant distribution and enhanced convective heat transfer.
- The evaluation of hydraulic performance indicates that the DINOS-CP is capable of achieving a maximum reduction in pressure drop of 34% when compared to the SF-CP.
- Overall cooling efficiency shows that the DINOS-CP required 60% less pumping power, compared to the SF-CP, to reach a $R_{c\text{-}in,max}$ of 0.032 °C/W.
- Benchmarking shows the DINOS-CP outperforms several existing cooling module designs in normalized thermal resistance and pumping power. This balance of enhanced heat removal and minimized hydraulic penalty makes it a promising solution for high-power electronic cooling applications.
- Use of soft metal TIM led to reductions in critical heater temperatures by up to 6.5% and thermal resistances by up to 11%, with up to 15% improvement in average heat transfer coefficient. The choice of TIM had minimal impact on hydraulic performance.

The DINOS-CP design, integrating the distributed inlet-outlet concept into a manufacturable cold plate, offers a practical and energy-efficient solution for high-power single-chip cooling. It is well-suited for GPUs, CPUs, and AI computing platforms, supporting low power usage effectiveness (PUE) and sustainable operation. Future work will focus on extending the DINOS-CP toward system-level deployment, including expanding to multi-heat-source architectures (e.g., ASICs), incorporating two-phase flow boiling for ultra-high heat-flux applications, and reliability-qualifying the electrochemically printed structure under long-term thermal cycling and operational loading conditions. These efforts will further advance the DINOS-CP toward next-generation, data-center-ready cooling solutions for high-power-density electronics.

Declaration of generative AI and AI-assisted technologies in the writing process

During the preparation of this work, the author(s) used GRAMMARLY in order to improve the readability of the manuscript. After using this tool/service, the author(s) reviewed and edited the content as needed and take(s) full responsibility for the content of the published article.

CRediT authorship contribution statement

Sangram Kumar Samal: Conceptualization, Methodology, Formal analysis, Data curation, Validation, Visualization, Investigation, Writing – original draft. **Pang-Chieh Yu:** Investigation, Data curation, Validation. **Hsien-Chun Chang:** Investigation, Data curation, Validation. **Yogesh Fulpagare:** Conceptualization, Methodology, Resources, Writing – review & editing. **Ian Winfield:** Methodology, Resources. **Michael Matthews:** Methodology, Resources. **Himanshu Pokharna:** Methodology, Resources. **Chi-Chuan Wang:** Conceptualization, Methodology, Supervision, Writing – review & editing, Funding acquisition.

Declaration of competing interest

The authors declare that they have no known competing financial interests or personal relationships that could have appeared to influence the work reported in this paper.

Acknowledgements

The authors wish to express their sincere appreciation for the financial support provided by Cooler Master Co., Ltd. in Taiwan and the National Science and Technology Council of Taiwan, under contract no. 114-2221-*E*-A49-165-MY3. Additionally, the authors would like to extend their gratitude to Deep Materials Inc., USA, for supplying the soft

metal thermal interface material (FlexiMetal) utilized in this experiment. The authors also acknowledge Fabric8Labs, Inc., USA, for their assistance with the 3D printing of the cold plate employing ECAM technology.

Appendix A. Supplementary data

Supplementary data to this article can be found online at https://doi.org/10.1016/j.applthermaleng.2026.130683.

Data availability

Data will be made available on request.

References

[1] X. Yuan, X. Zhou, Y. Pan, R. Kosonen, H. Cai, Y. Gao, Y. Wang, Phase change cooling in data centers: a review, Energ. Buildings 236 (2021) 110764, https://doi.org/10.1016/j.enbuild.2021.110764.
[2] Y. Zhang, K. Shan, X. Li, H. Li, S. Wang, Research and technologies for next-generation high-temperature data centers – state-of-the-arts and future perspectives, Renew. Sust. Energ. Rev. 171 (2023) 112991, https://doi.org/10.1016/j.rser.2022.112991.
[3] A. Habibi Khalaj, S.K. Halgamuge, A review on efficient thermal management of air- and liquid-cooled data centers: from chip to the cooling system, Appl. Energy 205 (2017) 1165–1188, https://doi.org/10.1016/j.apenergy.2017.08.037.
[4] blackwell-datasheet-4204213. https://nvdam.widen.net/s/wwnsxrhm2w/blackwell-datasheet-3384703, 2025 (accessed 20 November 2025).
[5] blackwell-datasheet-ultra-blackwell-4169750. https://resources.nvidia.com/en-us-blackwell-architecture/blackwell-ultra-datasheet?ncid=no-ncid, 2025 (accessed 20 November 2025).
[6] Y. Fulpagare, A. Bhargav, Advances in data center thermal management, Renew. Sust. Energ. Rev. 43 (2015) 981–996, https://doi.org/10.1016/j.rser.2014.11.056.
[7] M. Azarifar, M. Arik, J.-Y. Chang, Liquid cooling of data centers: a necessity facing challenges, Appl. Therm. Eng. 247 (2024) 123112, https://doi.org/10.1016/j.applthermaleng.2024.123112.
[8] R. Kong, H. Zhang, M. Tang, H. Zou, C. Tian, T. Ding, Enhancing data center cooling efficiency and ability: a comprehensive review of direct liquid cooling technologies, Energy 308 (2024) 132846, https://doi.org/10.1016/j.energy.2024.132846.
[9] Z. Li, H. Luo, Y. Jiang, H. Liu, L. Xu, K. Cao, H. Wu, P. Gao, H. Liu, Comprehensive review and future prospects on chip-scale thermal management: Core of data center's thermal management, Appl. Therm. Eng. 251 (2024) 123612, https://doi.org/10.1016/j.applthermaleng.2024.123612.
[10] N. Wang, Y. Guo, C. Huang, S. Shao, Advances in direct liquid cooling technology and waste heat recovery for data center: a state-of-the-art review, J. Clean. Prod. 477 (2024) 143872, https://doi.org/10.1016/j.jclepro.2024.143872.
[11] M. Khoshvaght-Aliabadi, P. Ghodrati, J.Y. Shin, Y.T. Kang, Impact of coolant distribution design on server-level thermal management in data centers, Energy 330 (2025) 136936, https://doi.org/10.1016/j.energy.2025.136936.
[12] Z. Wu, G. Zhang, S. Lu, P. Leng, Y. Yu, J. Deng, W. Huang, A comprehensive review of cold plate liquid cooling technology for data centers, Chem. Eng. Sci. 310 (2025) 121525, https://doi.org/10.1016/j.ces.2025.121525.
[13] B. Ramakrishnan, H. Alissa, I. Manousakis, R. Lankston, R. Bianchini, W. Kim, R. Baca, P.A. Misra, I. Goiri, M. Jalili, A. Raniwala, B. Warrier, M. Monroe, C. Belady, M. Shaw, M. Fontoura, CPU overclocking: a performance assessment of air, cold plates, and two-phase immersion cooling, IEEE Trans. Compon. Packag. Manuf. Technol. 11 (10) (2021) 1703–1715, https://doi.org/10.1109/TCPMT.2021.3106026.
[14] D.B. Tuckerman, R.F.W. Pease, High-performance heat sinking for VLSI (in English), Electron Devic Lett 2 (5) (1981) 126–129, https://doi.org/10.1109/EDL.1981.25367.
[15] X. Tan, H. Liu, J. Zhang, W. Tian, J. Yu, X. Ruan, B. Wang, L. Wu, J. Zhang, N. Ahuja, Investigation on advanced cold plate liquid cooling solution for large scale application in data center, in: *2023 22nd IEEE Intersociety Conference on Thermal and Thermomechanical Phenomena in Electronic Systems (ITherm)*, Orlando, FL, USA, 30 May 2023–02 June 2023 2023, IEEE, 2023, pp. 1–7, https://doi.org/10.1109/ITherm55368.2023.10177559.
[16] W. Zhou, K. Dong, Q. Sun, W. Luo, B. Zhang, S. Guan, G. Wang, Research progress of the liquid cold plate cooling technology for server electronic chips: a review, Int. J. Energy Res. 46 (9) (2022) 11574–11595, https://doi.org/10.1002/er.7979.
[17] S. Rangarajan, S.N. Schiffres, B. Sammakia, A review of recent developments in "On-Chip" embedded cooling technologies for heterogeneous integrated applications, Engineering 26 (2023) 185–197, https://doi.org/10.1016/j.eng.2022.10.019.
[18] B. Ramakrishnan, Y. Hadad, S. Alkharabsheh, P.R. Chiarot, B. Sammakia, Thermal analysis of cold plate for direct liquid cooling of high performance servers, J. Electron. Packag. 141 (4) (2019) 041005, https://doi.org/10.1115/1.4044130.
[19] Y. Hadad, N. Fallahtafti, L. Choobineh, C.H. Hoang, V. Radmard, P.R. Chiarot, B. Sammakia, Performance analysis and shape optimization of an impingement microchannel cold plate, IEEE Trans. Compon. Packag. Manuf. Technol. 10 (8) (2020) 1304–1319, https://doi.org/10.1109/TCPMT.2020.3005824.
[20] C. Gui, Y. Wang, C. Shen, S. Wang, R. Wang, Z. Lv, B. Lin, W. Tian, Z. Li, X. Zhang, K. Zhang, L. Wu, N. Ahuja, Advanced cold plate liquid cooling solution for hyper-scale data center application, in: *2023 22nd IEEE Intersociety Conference on Thermal and Thermomechanical Phenomena in Electronic Systems (ITherm)*, Orlando, FL, USA, 30 May 2023–02 June 2023 2023, IEEE, 2023, pp. 1–6, https://doi.org/10.1109/ITherm55368.2023.10177549.
[21] A. Heydari, A.R. Gharaibeh, M. Tradat, Q. soud, Y. Manaserh, V. Radmard, B. Eslami, J. Rodriguez, B. Sammakia, Experimental evaluation of direct-to-chip cold plate liquid cooling for high-heat-density data centers, Appl. Therm. Eng. 239 (2024) 122122, https://doi.org/10.1016/j.applthermaleng.2023.122122.
[22] S. Qu, K. Duan, Y. Guo, Y. Feng, C. Wang, Z. Xing, Real-time optimization of the liquid-cooled data center based on cold plates under different ambient temperatures and thermal loads, Appl. Energy 363 (2024) 123101, https://doi.org/10.1016/j.apenergy.2024.123101.
[23] J. Miao, C. Li, M. Pan, Experimental and numerical analysis of variable cross-section channel liquid cooling plate for server chips thermal management, Therm. Sci. Eng. Progr. 49 (2024) 102470, https://doi.org/10.1016/j.tsep.2024.102470.
[24] M. Matsuda, Y. Kawahara, Y. Horiuchi, Y. Tahara, Y. Saito, T. Tomitsuka, Thermal performance of transient liquid phase diffusion bonded multi-layer cold plate, in: *2024 23rd IEEE Intersociety Conference on Thermal and Thermomechanical Phenomena in Electronic Systems (ITherm)*, Aurora, CO, USA, 28–31 May 2024 2024, IEEE, 2024, pp. 1–7, https://doi.org/10.1109/ITherm55375.2024.10709444.
[25] D.J.G. Kuiphuis, M.J. Terpstra, W.W. Wits, W. Rohlfs, Thermal-hydrodynamic modeling and design for microchannel cold plates subjected to multiple heat sources, Appl. Therm. Eng. 262 (2025) 125220, https://doi.org/10.1016/j.applthermaleng.2024.125220.
[26] D. Beberide, M. Vilarrubí, J. Camarasa, D. Sancho, D. Regany, J. Barrau, Experimental evaluation of different cold plates configurations for direct-to-Chip liquid cooling, *2025 31st international workshop on thermal investigations of ICs and systems (THERMINIC)*, Naples, Italy, 24-26 September 2025, IEEE 2025 (2025) 1–6, https://doi.org/10.1109/THERMINIC65879.2025.11216931.
[27] A.M. Huber, R. Viskanta, Effect of jet-jet spacing on convective heat transfer to confined, impinging arrays of axisymmetric air jets, Int. J. Heat Mass Transf. 37 (18) (1994) 2859–2869, https://doi.org/10.1016/0017-9310(94)90340-9.
[28] G. Natarajan, R.J. Bezama, Microjet cooler with distributed returns, Heat Transfer Eng. 28 (8–9) (2007) 779–787, https://doi.org/10.1080/01457630701328627.
[29] A.J. Onstad, C.J. Elkins, R.J. Moffat, J.K. Eaton, Full-field flow measurements and heat transfer of a compact jet impingement array with local extraction of spent fluid (in English), J. Heat Transf. 131 (8) (Aug 2009) 082201, https://doi.org/10.1115/1.3109991.
[30] T.B. Hoberg, A.J. Onstad, J.K. Eaton, Heat transfer measurements for jet impingement arrays with local extraction, Int. J. Heat Fluid Flow 31 (3) (2010) 460–467, https://doi.org/10.1016/j.ijheatfluidflow.2010.01.009.
[31] C.U. Gonzalez-Valle, S. Samir, B. Ramos-Alvarado, Experimental investigation of the cooling performance of 3-D printed hybrid water-cooled heat sinks, Appl. Therm. Eng. 168 (2020) 114823, https://doi.org/10.1016/j.applthermaleng.2019.114823.
[32] T.W. Wei, H. Oprins, L. Fang, V. Cherman, I. De Wolf, E. Beyne, M. Baelmans, Nozzle scaling effects for the thermohydraulic performance of microjet impingement cooling with distributed returns, Appl. Therm. Eng. 180 (2020) 115767, https://doi.org/10.1016/j.applthermaleng.2020.115767.
[33] Y. Fan, X. Zhang, L. Xiang, Y. Cheng, X. Luo, A compact jet array impingement cooling system driven by integrated piezoelectric micropump, Int. J. Heat Mass Transf. 205 (2023) 123905, https://doi.org/10.1016/j.ijheatmasstransfer.2023.123905.
[34] Q. Liu, Q. Shi, X. Yao, C. Xu, M.M.A. El-Samie, X. Ju, Study of manifold micro-pin–fin heat sinks: application of rhombus-based topologies to organize three-dimensional flows, J. Therm. Anal. Calorim. 149 (1) (2023) 389–411, https://doi.org/10.1007/s10973-023-12713-0.
[35] G. Elsinger, H. Oprins, V. Cherman, G. Van der Plas, E. Beyne, I. De Wolf, Modeling-based improvement of microscale liquid jet impingement cooling, IEEE Trans. Compon. Packag. Manuf. Technol. 14 (7) (2024) 1180–1188, https://doi.org/10.1109/tcpmt.2024.3421585.
[36] G. Elsinger, H. Oprins, V. Cherman, G. Van der Plas, E. Beyne, I. De Wolf, Effects of nozzle pitch adaptation in micro-scale liquid jet impingement, Fluids 9 (3) (2024) 69, https://doi.org/10.3390/fluids9030069.
[37] A. Patel, G. Sahu, T. Wei, Heat transfer enhancement for direct-on-chip impingement jet cooling using variable micro pin fins and tapered impingement cavity, in: In *2024 23rd IEEE Intersociety Conference on Thermal and Thermomechanical Phenomena in Electronic Systems (ITherm)*, Aurora, CO, USA, 28-31 May 2024, IEEE, 2024, pp. 1–9, https://doi.org/10.1109/ITherm55375.2024.10709594.
[38] T. Wei, H. Oprins, V. Cherman, E. Beyne, M. Baelmans, Conjugate heat transfer and fluid flow modeling for liquid microjet impingement cooling with alternating feeding and draining channels, Fluids 4 (3) (2019) 145, https://doi.org/10.3390/fluids4030145.
[39] T.W. Wei, H. Oprins, V. Cherman, G. Van der Plas, I. De Wolf, E. Beyne, M. Baelmans, Experimental characterization and model validation of liquid jet impingement cooling using a high spatial resolution and programmable thermal test chip, Appl. Therm. Eng. 152 (2019) 308–318, https://doi.org/10.1016/j.applthermaleng.2019.02.075.
[40] R. Wu, Y. Fan, T. Hong, H. Zou, R. Hu, X. Luo, An immersed jet array impingement cooling device with distributed returns for direct body liquid cooling of high power

electronics, Appl. Therm. Eng. 162 (2019) 114259, https://doi.org/10.1016/j.applthermaleng.2019.114259.
[41] R. Kempers, J. Colenbrander, W. Tan, R. Chen, A.J. Robinson, Experimental characterization of a hybrid impinging microjet-microchannel heat sink fabricated using high-volume metal additive manufacturing, Int. J. Thermofluids 5-6 (2020) 100029, https://doi.org/10.1016/j.ijft.2020.100029.
[42] T. Brunschwiler, H. Rothuizen, M. Fabbri, U. Kloter, B. Michel, R.J. Bezama, G. Natarajan, Direct liquid jet-Impingment cooling with Micron-sized nozzle Array and distributed return architecture, in: Thermal and Thermomechanical Proceedings 10th Intersociety Conference on Phenomena in Electronics Systems, 2006. ITHERM 2006., San Diego, CA, USA, 30 May 2006–02 June 2006, IEEE, 2006, pp. 196–203, https://doi.org/10.1109/ITHERM.2006.1645343.
[43] A.S. Rattner, General characterization of jet impingement Array heat sinks with interspersed fluid extraction ports for uniform high-flux cooling, J. Heat Transf. 139 (8) (2017) 082201, https://doi.org/10.1115/1.4036090.
[44] L.E. Paniagua-Guerra, S. Sehgal, C.U. Gonzalez-Valle, B. Ramos-Alvarado, Fractal channel manifolds for microjet liquid-cooled heat sinks, Int. J. Heat Mass Transf. 138 (2019) 257–266, https://doi.org/10.1016/j.ijheatmasstransfer.2019.04.039.
[45] T. Wei, H. Oprins, V. Cherman, J. Qian, I. De Wolf, E. Beyne, M. Baelmans, High-efficiency polymer-based direct multi-jet impingement cooling solution for high-power devices, IEEE Trans. Power Electron. 34 (7) (2019) 6601–6612, https://doi.org/10.1109/TPEL.2018.2872904.
[46] T. Wei, H. Oprins, V. Cherman, Z. Yang, K.C. Rivera, G.V. d. Plas, B.J. Pawlak, L. England, E. Beyne, M. Baelmans, Experimental and numerical study of 3-D printed direct jet impingement cooling for high-power, large die size applications, IEEE Trans. Components Packag. Manuf. Technol. 11 (3) (2021) 415–425, https://doi.org/10.1109/tcpmt.2020.3045113.
[47] R. Moloudi, T. Grün, W. Verleysen, B. Vandevelde, S.G.C. Cleuren, D. May, B. Wunderle, Metal-based direct multi-jet impingement cooling solution for autonomous driving high-performance vehicle computer (HPVC), in: In *2023 24th International Conference on Thermal, Mechanical and Multi-Physics Simulation and Experiments in Microelectronics and Microsystems (EuroSimE)*, Graz, Austria, 16-19 April 2023, IEEE, 2023, pp. 1–6, https://doi.org/10.1109/EuroSimE56861.2023.10100758.
[48] G. Elsinger, H. Oprins, V. Cherman, G. Van der Plasv, E. Beyne, I. De Wolf, Enhancement of direct liquid jet impingement cooling through laser-fabricated micro pin-fins on the chip-backside, in: In *2024 23rd IEEE Intersociety Conference on Thermal and Thermomechanical Phenomena in Electronic Systems (ITherm)*, Aurora, CO, USA, 28-31 May 2024, IEEE, 2024, pp. 1–10, https://doi.org/10.1109/ITherm55375.2024.10709578.
[49] G. Sahu, R. Li, K. Yogi, A. Patel, T. Wei, Experimental investigation of a compact lid-compatible multi-jet impingement manifold for direct-on-chip cooling, IEEE Trans. Compon. Packag. Manuf. Technol. (2024) 748–756, https://doi.org/10.1109/tcpmt.2024.3506943.
[50] A. Patel, K. Yogi, G. Sahu, T. Wei, Multi-chip jet impingement cooling for heat dissipation in 2.5D integrated system with 1 kW+ thermal design power, Int. J. Heat Mass Transf. 244 (2025) 126978, https://doi.org/10.1016/j.ijheatmasstransfer.2025.126978.
[51] M. Frank, M. Matthews, J. Madril, I. Winfield, Electrochemical additive manufacturing: A novel approach to thermal management of electronics, in: 2023 *IEEE 73rd Electronic Components and Technology Conference (ECTC)*, Orlando, FL, USA, 30 May 2023–02 June 2023 2023, IEEE, 2023, pp. 432–436, https://doi.org/10.1109/ECTC51909.2023.00078.
[52] J. Lamotte-Dawaghreh, J. Herring, G. Gupta, D. Agonafer, J. Madril, T. Ouradnik, I. Winfield, M. Matthews, CFD study of electrochemical additive manufacturing based cold plate designs for enhanced electronics cooling, in: *2024 23rd IEEE Intersociety Conference on Thermal and Thermomechanical Phenomena in Electronic Systems (ITherm)*, Aurora, CO, USA, 28–31 May 2024 2024, IEEE, 2024, pp. 1–8, https://doi.org/10.1109/ITherm55375.2024.10709617.
[53] G. Gupta, D. Castro, J. Madril, T. Ouradnik, I. Winfield, M. Matthews, D. Agonafer, Numerical and experimental investigation of high-powered chips for efficient cooling using optimized electrochemical additive manufacturing based cold plates, in: *2025 24th IEEE Intersociety Conference on Thermal and Thermomechanical Phenomena in Electronic Systems (ITherm)*, Dallas, TX, USA, 27–30 May 2025 2025, IEEE, 2025, pp. 1–7, https://doi.org/10.1109/ITherm55376.2025.11235654.
[54] S.K. Samal, H.-C. Chang, Y. Fulpagare, C.-C. Wang, Thermal management of data centers: Chip-scale cooling using novel distributed inlet–outlet jet impingement liquid cold plate, Appl. Therm. Eng. 271 (2025) 126360, https://doi.org/10.1016/j.applthermaleng.2025.126360.
[55] S.K. Samal, C.-C. Wang, Y. Fulpagare, Novel multi-nozzle jet impingement liquid cold plate for cooling of high-power density electronic chip, in: *2025 24th IEEE Intersociety Conference on Thermal and Thermomechanical Phenomena in Electronic Systems (ITherm)*, Dallas, TX, USA, 27–30 May 2025 2025, IEEE, 2025, pp. 1–7, https://doi.org/10.1109/ITherm55376.2025.11235746.
[56] Cooler Master CryoFuze 7 Thermal Paste. https://www.coolermaster.com/en-global/products/cryofuze-7/?tab=overview, 2025 (accessed 17 November, 2025).
[57] Deep Materials ELM, FlexiMetal TIMs. https://www.deep-materials.com/Products/FlexiMetal-and-ELM-Products.html, 2025 (accessed 17 November, 2025).
[58] C. Chen, D. Trieu, T. Shah, A. Guo, J. Cheng, C. Chapman, S. Kang, E. Dagan, A. Dinstag, J. Yao, OCP OAI system liquid cooling guidelines, in: Open Compute Project, 2023 [Online]. Available: https://www.opencompute.org/documents/oai-system-liquid-cooling-guidelines-in-ocp-template-mar-3-2023-update-pdf.
[59] V.A. Martinez, C. Caceres, A. Ortega, Development of a thermal metrology standard for evaluation of cold plate thermal resistance as a performance metric, J. Electron. Packag. 146 (4) (2024) 041118, https://doi.org/10.1115/1.4066101.
[60] C. Chen, Y. Hang, N. Mithani, C. Malone, Y. Li, W. Zhang, J. Fernandes, K. Dhake, J. Wyatt, J. Clow, D. Young, OCP Practices and insights into Liquid Cooling on Meta's AI Training Platforms [Online]. Available: https://www.opencompute.org/documents/practices-and-insights-into-liquid-cooling-on-metas-ai-training-platforms-ocp-format-august-14-2023-pdf, 2023.